

3D numerical modeling and experimental validation of machining Nomex® honeycomb materials

Mohamed Jaafar, Mohammed Nouari, Hamid Makich, Abdelhadi Moufki

▶ **To cite this version:**

Mohamed Jaafar, Mohammed Nouari, Hamid Makich, Abdelhadi Moufki. 3D numerical modeling and experimental validation of machining Nomex® honeycomb materials. International Journal of Advanced Manufacturing Technology, 2021, 115 (9-10), pp.2853-2872. 10.1007/s00170-021-07336-4 . hal-03325745

HAL Id: hal-03325745
https://hal.univ-lorraine.fr/hal-03325745

Submitted on 2 Feb 2022

HAL is a multi-disciplinary open access archive for the deposit and dissemination of scientific research documents, whether they are published or not. The documents may come from teaching and research institutions in France or abroad, or from public or private research centers.

L'archive ouverte pluridisciplinaire **HAL**, est destinée au dépôt et à la diffusion de documents scientifiques de niveau recherche, publiés ou non, émanant des établissements d'enseignement et de recherche français ou étrangers, des laboratoires publics ou privés.

3D Numerical modeling and experimental validation of machining Nomex® honeycomb materials

Mohamed JAAFAR[1], Mohammed NOUARI[1,*], Hamid MAKICH[1], Abdelhadi MOUFKI[1]

[1]*Université de Lorraine, CNRS, LEM3, IMT, GIP InSIC, F-88100 Saint Dié des Vosges, France.*
[2]*Université de Lorraine, CNRS, Arts et Métiers ParisTech LEM3 F-57070 Metz, France.*

[*] Corresponding author: Mohammed NOUARI, Email address: mohammed.nouari@univ-lorraine.fr
Tel.: +33 (0)329 421 821; fax: +33 (0)329 421 825.

Abstract

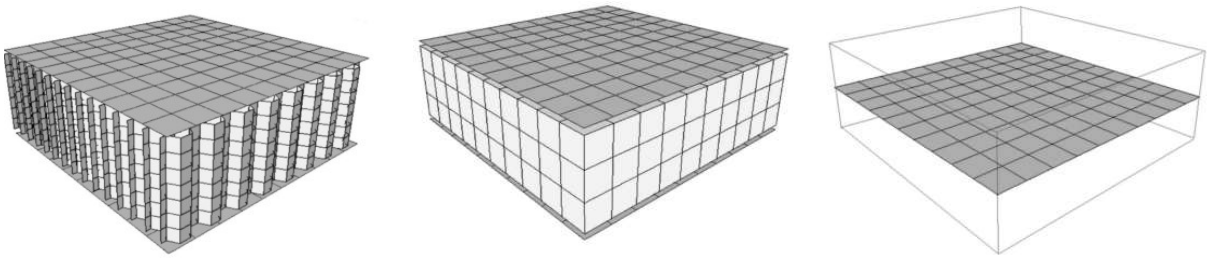
Machining of Nomex® honeycomb materials is the biggest challenge in industry because of the complex forms and geometry of the honeycomb structure. The latter is characterized by a low density with orthotropic mechanical behavior. The thin walls of the composite structure make the shaping of this material very difficult. Studying interactions between the cutting tool and material, cutting forces and chip formation allow to understand the machining process of Nomex® honeycomb. This paper presents 3D numerical modeling of machining Nomex® honeycomb using different orthotropic approaches and failure criteria : (i)- monolayer isotropic approach, (ii)- monolayer orthotropic approach with Tsai-Wu failure criteria and (iii)- monolayer orthotropic approach with Hashin failure criteria. A comparison between experiments and numerical cutting forces was performed to validate the proposed model. The interaction between the tool and the honeycomb walls, which make it possible to observe the different stages of the chip formation process, was carefully modeled.

Keywords: honeycomb structure; composite; Nomex®; machining; Hashin and Tsai-Wu failure criteria

1. Introduction

Due to their mechanical performance and light weight, sandwich materials with honeycomb core are widely used in the aerospace and automotive industry, they are employed for the aircraft doors, helicopter propeller and nosecone structure of formula 1, [1]. There are two wide variety of honeycombs, metallic (aluminum, titanium or steel) and composite (Nomex® with glass fibers or carbon fibers). The choice of honeycomb material depends on properties and specific benefits of each material. Nomex® is the most non-metallic honeycomb used as core of sandwich structures, it is composed of phenolic resin impregnated aramid paper, [2].

The honeycomb structure is characterized by orthotropic behavior with better resistance in out-of-plane compression [3–6], this behavior is primarily related to the alveolar geometric design of the structure and to the intrinsic behavior of aramid paper. To better understand the mechanical behavior of honeycomb structures under different solicitations, several studies have been interested to the modeling of this type of materials. There are three approaches used in the literature of honeycomb structures: (i)- mesomodels, (ii)- homogenized models and (iii)- shell models [7], see Figure 1.



(a) (b) (c)

Figure 1. Honeycomb structures considered with : (a) mesomodel; (b) homogenized model; and (c) shell model, [7].

The mesomodels are based on a detailed presentation of the honeycomb structure, getting as close as possible to reality with the walls modeled as shell elements. The advantage of this model is the ability to accurately map the states of the walls deformation in order to observe the damage suffered during loading, [8–10]. Given the high number of elements in mesomodels,

this modeling requires a high computation time in numerical simulations, [11]. An alternative approach is to homogenize the honeycomb structure and model it with 3D solid elements, for example 8-node hexahedron elements (C3D8R), [12–14]. The mechanical properties are assigned to these elements so that the homogenized structure behaves in the same way as the overall cell structure. The damage suffered by the structure and the failure modes of the material were not be clearly represented, [15]. A third simplification was proposed with a representation of the whole structure with shell elements, see Figure 1(c). In this case, the properties of the honeycomb are generally attributed to the integration points in the direction of the element thickness, [7,16].

The mesomodel is the most used model given the information and the results that it provides. This model consists of representing the honeycomb structure while respecting the real geometry of cells. Thus, to accomplish this model, the mechanical behavior of the paper is attributed to the walls of the structure, [17].

Knowing that Nomex® is manufactured with composite paper made of aramid fibers and phenolic resin, four modeling approaches have been developed in the literature, Figure 2. The first is to model the Nomex® paper walls as a monolayer with an isotropic elastoplastic behavior, [18–22]. This model is known for its simplicity and reduction in terms of the computation time. On the other hand, it does not represent the true mechanical behavior of the composite material, which is known by its orthotropic behavior due to the presence of fibers and resin, thus it neglects the composite architecture of the Nomex® paper. For this, the second approach models the walls as monolayers with orthotropic behavior [2,23–26]. This second method presents more possibilities of integration of damage laws and rupture modes. In the third approach, Nomex® paper is modeled using a multilayer structure based on the laminate theory by the representation of three layers, two layers of resin wrapping a layer of aramid fibers, with isotropic behavior for phenolic resin coating. Aramid paper can be modeled as an

isotropic or orthotropic material [2,27,28]. The last approach is based on the idea of representing more details with the modeling of resin accumulation on the Nomex® honeycomb cell junctions, [11,23]. This is achieved by combining the multilayer approach with additional elements on junctions to represent the accumulation of the resin. A mechanical behavior of the components similar to that of the previous approach is used for this modeling.

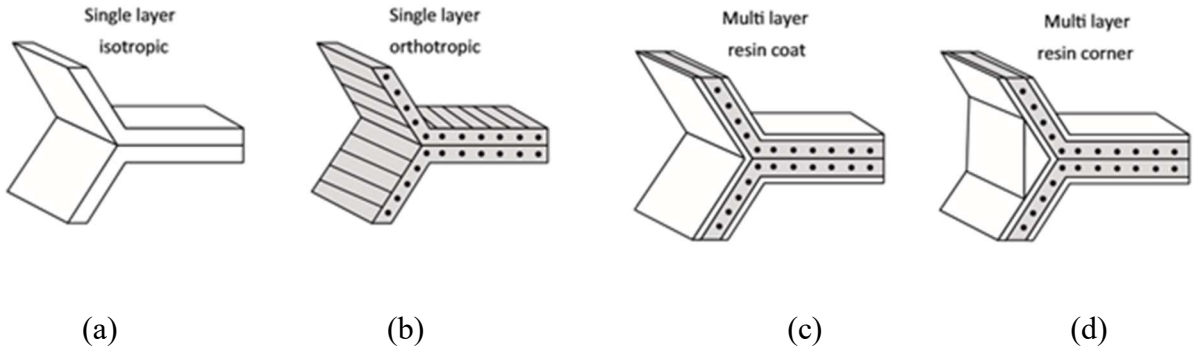


Figure 2. Nomex® paper modeling approaches. (a) Isotropic monolayer; (b) orthotropic monolayer; (c) multilayer; (d) multilayer with resin at the junctions, [23].

To observe the cell wall deformation and failure modes, Heimbs developed a model in [25] to predict the mechanical behavior of different honeycomb structures in off-plane compression using a mesomodel approach. He attributed a linearly orthotropic-perfectly plastic behavior to the Nomex® walls. In order to predict low-velocity impact response of the Nomex® honeycomb, Foo *et al.* [18] attributed an isotropic elastic perfectly-plastic behavior to the honeycomb walls. Similarly, Asprone *et al.* [29] attributed isotropic and linearly elasto-perfectly plastic to failure behavior of the walls of Nomex®. The sensitivity of these structures to material defects under crushing test was particularly analyzed. Besides, there are many studies that describe the Nomex® paper as a fragile composite material, [30–32]. This fragility is due to the phenolic resin which coats the aramid fibers, [24,33]. Indeed, Nomex® walls are characterized by local fragile elastic behavior and the rupture of the resin causes the failure of walls.

However, the interaction between the cutting tool and the honeycomb walls remains difficult to understand. The use of modeling and numerical simulation of machining facilitates the comprehension of this interaction. Honeycomb composites have been modeled by several authors under different types of mechanical loading, [6,23,32]. The proposed approaches generally allow to understand the damage mechanisms under different solicitations: tension, compression, shearing, etc. and the identification of parameters influencing their mechanical behavior. Using the DEFORM software Qiu *et al.* [34], simulated the interaction between a milling tool tooth and a single wall of aluminum honeycomb cell to observe the cutting mechanisms. The aim of their numerical model is to analyze the influence of the change in the contact position of the cell wall on the cutting tool for a single honeycomb wall. In addition, to consider the case where several honeycomb cell walls participate in the cutting process, the authors have supposed that during milling process the shape of the honeycomb cell does not differ from a regular hexagon and no severe cell wall collapse has occurred. The model does not take into account the effect of the flexibility of the adjacent cells which affects the quality of the machined surface.

Recently, Sun et al. [35] have been developed with ABAQUS software a 3D FE model of ultrasonic cutting for aluminum honeycomb by a disc cutter. In the thin cell walls, the constitutive behavior of workpiece material has been modelled by the Johnson Cook law. To consider the degradation of material stiffness, an accumulating damage model considering damage evolution has been introduced from the Johnson-Cook fracture criterion. Despite the particularity of the process studied, namely the interaction between the disc cutter and the thin cell walls, the authors have used the same approach as in conventional machining for the behavior and damage of the machined material. In addition, the simulations were limited to a workpiece with only few cells.

Compared to the existing models in the literature, our 3D approach takes into account several cells and their flexibility around the cutting zone. To do this, the management of the tool-cell contact has been optimized by breaking down the part into several blocks. The blocks concerned by the contact are activated as the tool advances in the part and becomes close to these blocks. This allows to simulate the cutting process for parts with a large number of cells and to analyze different tool geometries. Moreover, the proposed approach allows an easy processing protocol to analyse both local and global mechanical fields such as deformations, stresses, induced damage, and cutting forces. Most of these fields are not accessible via experimental tests. The proposed approach can then offer a very effective numerical tool for the analysis of physical phenomena involved during machining honeycomb materials. It can also be a helpful method to optimize the tool geometry and cutting conditions.

From an industrial point of view, the 3D FE model is able, in one hand to accurately simulate (with reasonable computation time) the real 3D milling operation with a cutting tool having a complex geometry (industrial tools), and on the other hand, to finely analyze the interactions between the honeycomb structure and the milling cutter according to the machining conditions.

2. Numerical modelling set up and experimental tests

The finite element code ABAQUS/EXPLICIT was used to simulate the milling operation of the Nomex® honeycomb material. Constitutive behavior laws are implemented in a user-defined subroutine VUMAT. In this section, the 3D milling operation is particularly considered, the results carried out with the proposed finite element model are compared to experimental results obtained from Nomex® machining tests.

2.1. Cutting tool and Nomex® honeycomb materials

There are several tools available for machining honeycombs : standard and specific cutting tools depending on the selected workpiece material and the desired cutting operation (grooving, surfacing, trimming, and drilling). The case study of this work concerns the milling of Nomex® honeycomb. The used milling cutters are provided from our partner 'Evatec Tools' Company, the main geometrical characteristics are described in Figure 3. This combined tool is composed of two parts designed for surfacing/dressing machining operation. The first part is a cutter body made of high-speed steel with 16 mm in diameter and having ten helixes with a chip breaker. This tool part is designated by the 'Shredder'. The second part is a circular cutting blade made of tungsten carbide with a diameter of 18.3 mm and having a rake angle of 22° and a flank angle of 2.5°.

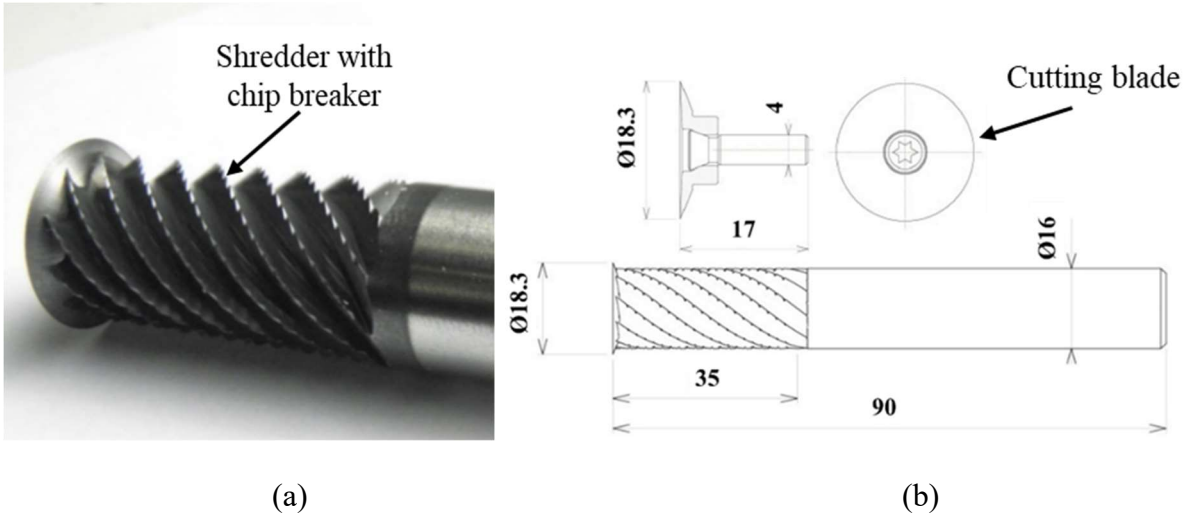


Figure 3. Milling tool designed by Evatec tools® company with reference NACNA 011 used for Nomex® honeycomb structures. (a)- Combined milling cutter. (b)- The 'Shredder' part with chip breaker made of high-speed steel and tungsten carbide cutting blade.

In our finite element model, the tool is modeled as a rigid material, which means the non-attribution of any mechanical or thermal properties to its material, so just the outer surface is retained as shown in Figure 4. The cutting tool is represented by a reference point located on its revolution axis. The cutting conditions are applied to the tool via its reference point with a feed rate in the X direction and a rotational speed around the Z axis. For this type of behavior (rigid behavior), the mesh of the tool must be provided to perform in a subsequent step the tool-

material contact. The mesh employed in this study is made of rigid 4-node quadrangular elements "R3D4" usually used for three-dimensional analyzes.

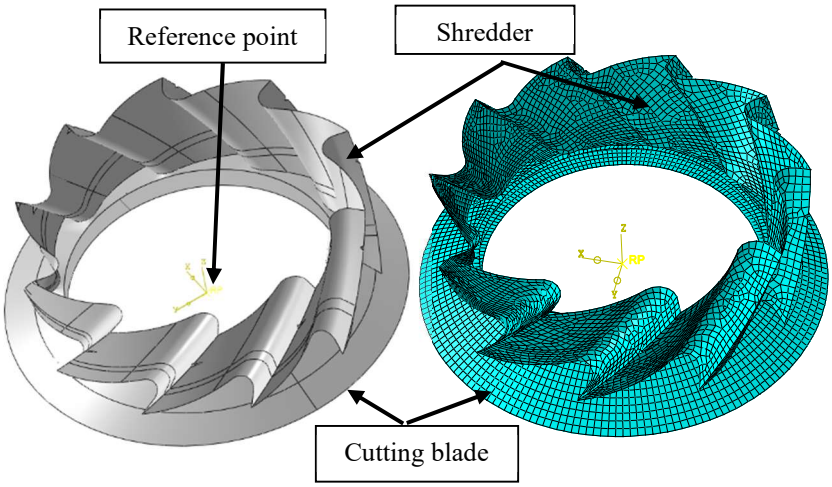
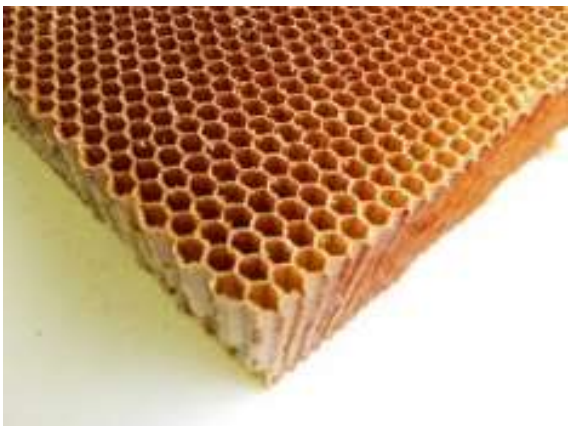
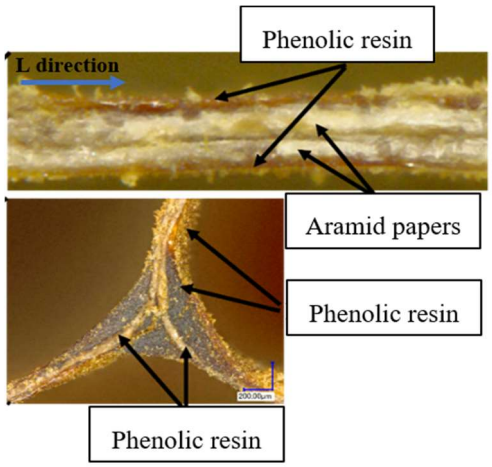


Figure 4. Combined tool showing the shredder and the cutting blade.

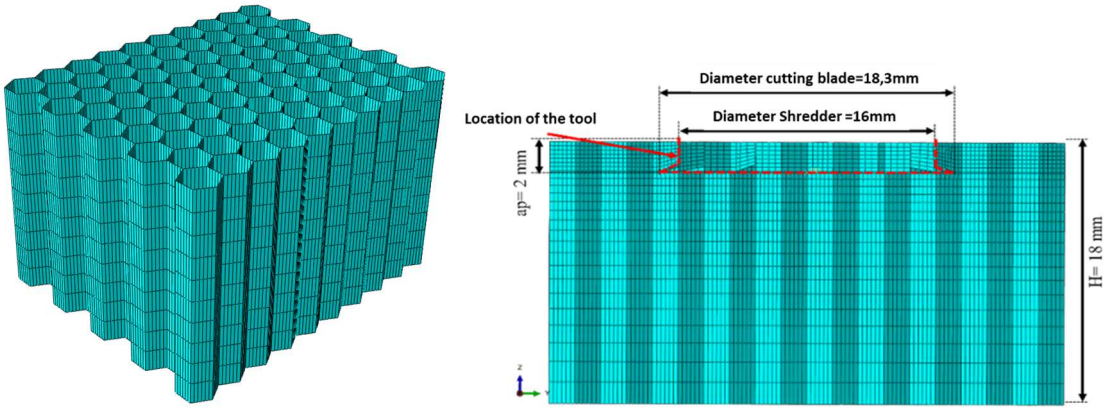
The workpiece material is the Nomex® honeycomb cores with thin cell walls. It is produced from aramid fiber dipped in phenolic resin (see Figures 5(a) and 5(b)). The chosen Nomex® has a density of 48 kg/m^3. The cells are 9.2 mm in size with a wall thickness of 80µm and the commercial reference of Nomex® is 'A10-48-3'.



(a)



(b)



(c) (d)

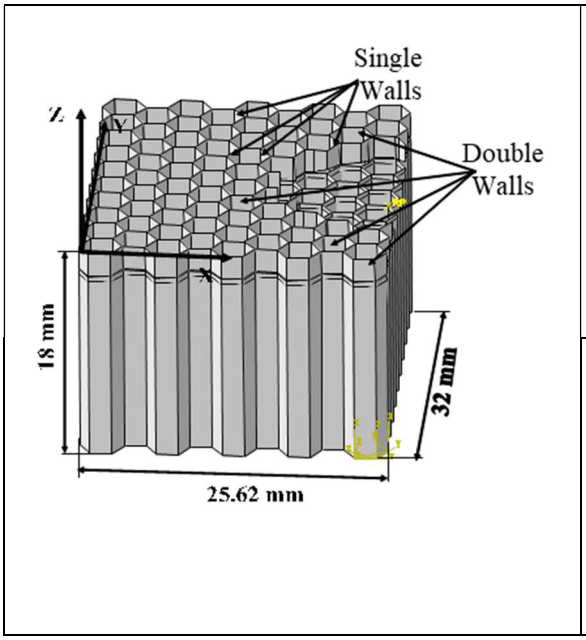
Figure 5. (a)- Nomex® honeycomb workpiece. (b)- Honeycomb cores with thin cell walls. (c)- Meshed composite structure. (d)- Honeycomb workpiece with the tool location.

All cells of Nomex® honeycomb are meshed with conventional shell elements with 4 nodes propertied 6 DOF / node (three displacements and three rotations) with a reduced integration "S4R", see Figure 5 (c). It is interesting to know that double honeycomb walls are two single walls linked together by a thin layer of adhesive. For simulations, the double walls are represented by a single shell element with double thickness. To reduce the CPU time, an initial tool engagement was defined as shown in Figure 5(d). The aim is to ensure a complete contact between the tool and the material structure at the beginning of the simulation. Moreover, the initial engagement is designed in consideration of the particular geometry of the milling cutter (cutting blade and shredder).

The experimental machining tests performed on honeycomb structures are grooving tests. For numerical simulations, boundary conditions were applied on the tool and the honeycomb workpiece in such a way to approach the experimental tests.

2.2. Cutting tests

For numerical simulations, the chosen dimensions of the honeycomb structure are as follows: (32 x 25.62 x 18 mm) which represents 19 rows of cells across the width and 9 rows of cells along the length, the geometric characteristics of the sample are presented in Figure 6.



Designation	A10-48-3
Density [Kg/m^3]	48
Cell size D [mm]	3.2
Wall size h [mm]	1.82
Wall thickness t [μm]	60
Angle α [°]	120

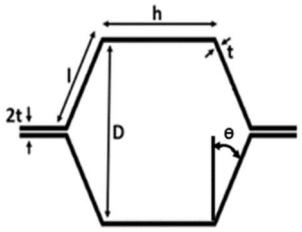
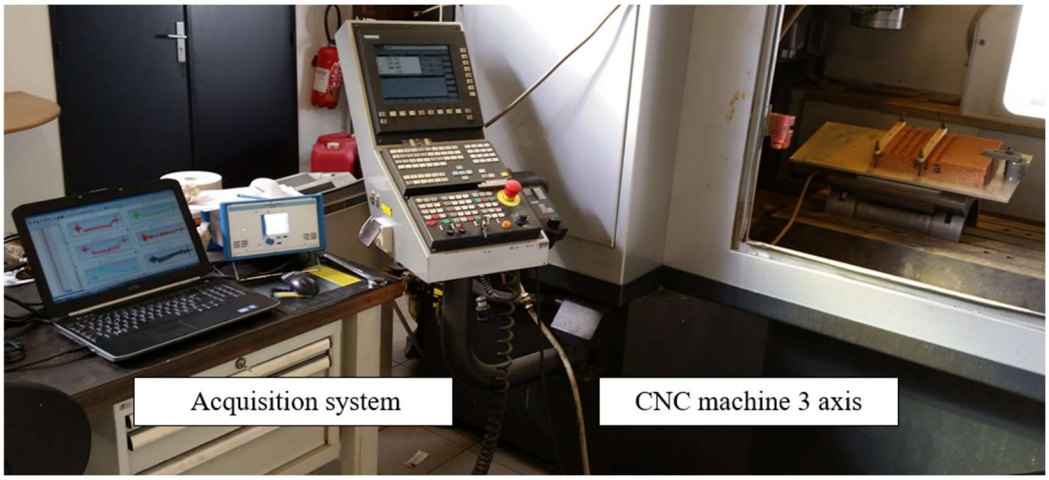
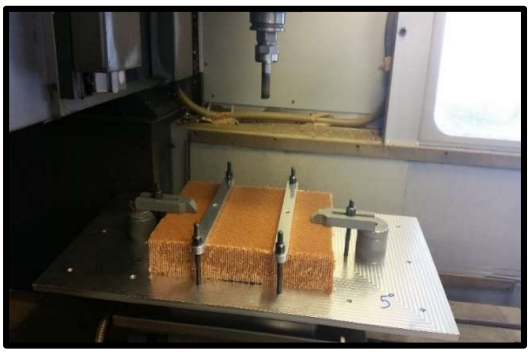


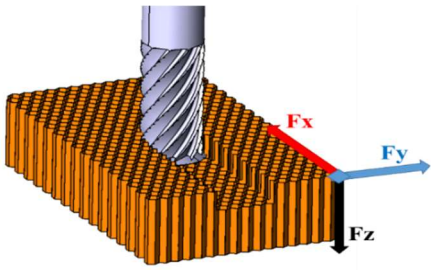
Figure 6. Scheme and mesh detail of the honeycomb structure (left side), geometric parameters of corresponding cells (right side).

Experimental milling tests were carried out on a three-axis vertical machining center. The main technical specifications of this machine are the maximum spindle speed of 24000 rpm, a power spindle motor of 30 KW, a maximum cutting feed rate of 20 m/min and a worktable area of 800 x 600 mm², see Figure 7. For assessing the performance of the machining process of Nomex® honeycomb, it is essential to monitor and measure the cutting forces generated during cutting. Therefore, the cutting forces were measured during the milling operation using Kistler dynamometer model 9129AA. The Kistler table is mounted below the Nomex® honeycomb sample to measure the three components of the machining force. Furthermore, during forces measurements, the x-axis of the dynamometer is aligned with the feed direction of the milling machine and the longitudinal direction of the workpiece (parallel to core ribbons and the direction of honeycomb double wall).



(a)





(b)

Figure 7. Experimental test setup on the three-axis vertical machining center. (a)- Instrumentation and acquisition system. The characteristics of the machine-tool are: maximum spindle speed of 24000 rpm, power spindle motor of 30 KW, maximum cutting feed rate of 20 m/min and a worktable area of 800 x 600 mm². (b)- Workpiece Fixing and cutting directions.

Regarding the contact between the cutting tool and Nomex honeycomb workpiece, two contacts areas must be considered in machining simulation. The first contact is that of the honeycomb walls coming into contact with the tool during its movement, for this contact a low friction value was chosen ($\mu = 0.1$). The choice of this low friction value can be explained by the small thickness of the honeycomb walls which minimizes the contact area with the cutting tool, thus, the alveolar geometry of the structure makes the friction discontinuous and weak. Other authors also used low values of friction for these kind of materials as Qiu et al. [34] who did simulations with a value of 0.2. In our study, we tested different values of friction between 0.1 and 0.25, the results showed a negligible influence of this variation on cutting forces. A second contact

can also occur between the walls themselves because of the folding thereof after the passage of the tool between the generated chip and the unmachined walls.

2.3. Material behavior and failure criteria

2.3.1. Monolayer isotropic law

Several authors have attributed to the Nomex® paper an isotropic elastoplastic behavior law, [24,25,36]. This behavior is well known by the simplicity of its implementation in numerical codes. Figure 8 shows the mechanical behavior of the Nomex® paper determined by Foo *et al.* [3] and Roy *et al*. [24]. The curves show a different elastic limit and plastic behavior depending on the thickness of the wall. Thus, the elastoplastic behavior attributed to the walls of honeycombs will depend on their thickness (single or double walls).

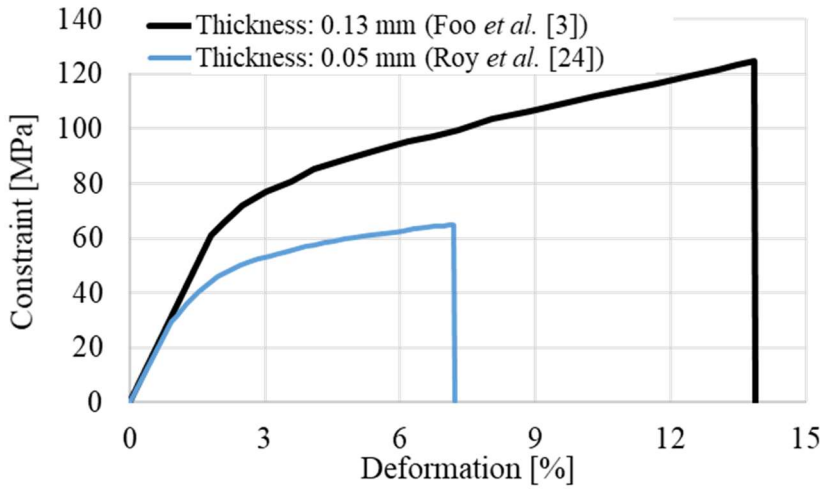


Figure 8. Stress-deformation curves for Nomex® T410 paper, [3,24].

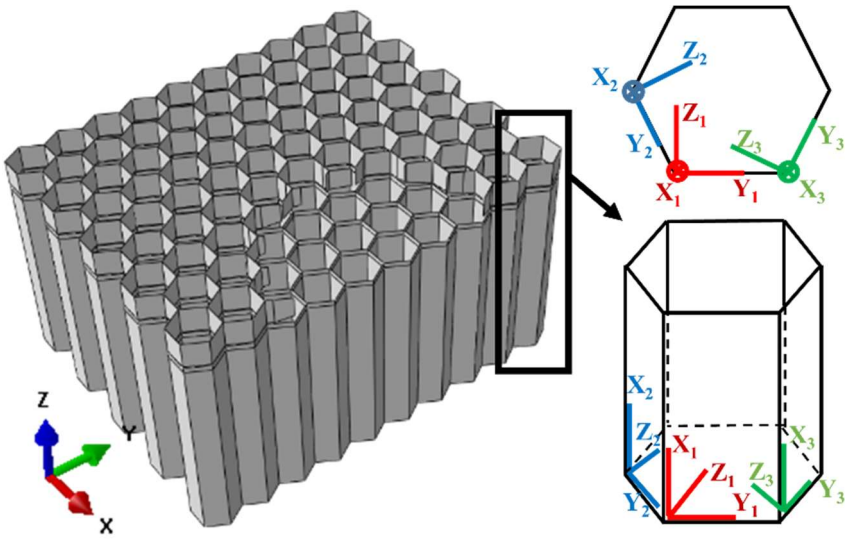
The mechanical properties attributed to Nomex® paper are given in Table 1.

Table 1. Mechanical properties of Nomex® paper, [3,24].

Mechanical properties	
Density (g/cm^3)	1.4
E (MPa)	3180
Poisson's ratio	0.3
Yield strengths for simple wall thickness (MPa)	29
Yield strengths for double wall thickness (MPa)	61

2.3.2. Monolayer orthotropic approach with Tsai-Wu failure criterion

Due to the alveolar geometry of the honeycomb structure and the assignment of the orthotropic mechanical property to each wall of honeycomb cells, a local reference has been defined for each cell walls orientation, see Figure 9.



(a) (b)

Figure 9. (a) Global reference (xyz). (b) Local references (X_1, Y_1, Z_1), (X_2, Y_2, Z_2), and (X_3, Y_3, Z_3).

Depending on the direction of the wall, a secondary reference has been defined for each cell walls orientation. In each local reference, the linear elasticity relation is written in the following form :

$$\{\varepsilon\} = \left[H^0\right]\{\sigma\} \qquad \text{Eq.1}$$

where $\{\varepsilon\}$ and $\{\sigma\}$ are the strain and stress tensors, respectively. $[H^0]$ is the matrix rigidity.

$$\begin{pmatrix} \varepsilon_{11} \\ \varepsilon_{22} \\ \varepsilon_{33} \\ \varepsilon_{23} \\ \varepsilon_{31} \\ \varepsilon_{12} \end{pmatrix} = \begin{pmatrix} \frac{1}{E_{11}} & -\frac{\upsilon_{12}}{E_{11}} & -\frac{\upsilon_{13}}{E_{11}} & 0 & 0 & 0 \\ -\frac{\upsilon_{21}}{E_{22}} & -\frac{1}{E_{22}} & -\frac{\upsilon_{23}}{E_{22}} & 0 & 0 & 0 \\ -\frac{\upsilon_{31}}{E_{33}} & -\frac{\upsilon_{32}}{E_{33}} & \frac{1}{E_{33}} & 0 & 0 & 0 \\ 0 & 0 & 0 & \frac{1}{G_{23}} & 0 & 0 \\ 0 & 0 & 0 & 0 & \frac{1}{G_{13}} & 0 \\ 0 & 0 & 0 & 0 & 0 & \frac{1}{G_{12}} \end{pmatrix} \begin{pmatrix} \sigma_{11} \\ \sigma_{22} \\ \sigma_{33} \\ \sigma_{23} \\ \sigma_{31} \\ \sigma_{12} \end{pmatrix} \quad \text{Eq.2}$$

with symmetry we have :

$$\frac{\upsilon_{21}}{E_{22}} = \frac{\upsilon_{12}}{E_{11}}, \frac{\upsilon_{31}}{E_{33}} = \frac{\upsilon_{13}}{E_{11}}, \frac{\upsilon_{32}}{E_{33}} = \frac{\upsilon_{23}}{E_{22}} \quad \text{Eq. 3}$$

E_{ii}, G_{ij}, υ_{ij} are the elastic modulus, shear modulus, and Poisson's ratio, respectively.

The orthotropic mechanical properties of the Nomex® paper shown in Table 2 are taken from the work conducted by Kilchert, [27].

Table 2. Orthotropic mechanical properties of Nomex® paper, [27].

Mechanical properties	
Density (g/cm^3)	1.4
E_{11} (MPa)	9200
E_{22} (MPa)	8300
E_{33} (MPa)	4700
G_{12} (MPa)	2600
G_{13}, G_{23} (MPa)	1700
υ_{12}, υ_{13}, υ_{23}	0.35
Ultimate strength	
Longitudinal tensile strength (MPa) : X_t	111
Longitudinal compressive strength (MPa): X_c	53
Transverse tensile strength (MPa) : Y_t	98
Transverse compressive strength (MPa) : Y_c	47
In-plan shear strength (MPa) : S_{12}	59
Inter-laminar shear strength (MPa) : S_{23}	159

The composite nature of the Nomex® paper requires the definition of failure criteria. These criteria make it possible to evaluate the resistance of the material under multiaxial loadings

from the mechanical strengths. There are several criteria of rupture that can be found in the literature, they are classified in three categories [37,38] : limit criteria, interactive criteria and independent criteria. The criterion of Tsai Wu is an interactive criterion which represents a generalization of the Von Mises criterion for the case of isotropic materials. The Tsai-Wu failure criteria have the following form as shown by Equations 4 and 5 :

$$F_{11}\sigma_1^2 + F_{22}\sigma_2^2 + F_{33}\sigma_3^2 + F_{44}\sigma_{23}^2 + F_{55}\sigma_{13}^2 + F_{66}\sigma_{12}^2 + 2F_{12}\sigma_1\sigma_2 + 2F_{13}\sigma_1\sigma_3 + 2F_{23}\sigma_2\sigma_3 + F_1\sigma_1 + F_2\sigma_2 + F_3\sigma_3 = 1 \quad \text{Eq. 4}$$

with

$$F_{11} = \frac{1}{X_t X_c};\ F_1 = \frac{1}{X_t} - \frac{1}{X_c};\ F_{33} = F_{22} = \frac{1}{Y_t Y_c}$$
$$F_3 = F_2 = \frac{1}{Y_t} - \frac{1}{Y_c};\ F_{44} = \frac{1}{(S_{23})^2};\ F_{55} = F_{66} = \frac{1}{S_{12}{}^2} \quad \text{Eq. 5}$$
$$F_{13} = F_{12} = -\frac{1}{2}\sqrt{F_{11}F_{22}};\ F_{23} = -\frac{1}{2}\sqrt{F_{22}F_{33}}$$

σ_{ij} are the principal stress (expressed in the local material coordinates systems (1, 2, 3) as illustrated in Figure. 9). F_i, F_{ij} are the second order and fourth strength tensors, and i, j = 1,..,6. S_{12} is the 'in-plan' shear strength and S_{23} the inter-laminar shear strength. X_t and X_c are the longitudinal tensile strength and longitudinal compressive strength, respectively. Y_t and Y_c are the transverse tensile strength and transverse compressive strength, respectively.

2.3.3. Monolayer orthotropic approach with Hashin failure criteria

The Hashin failure criteria have also been chosen by several authors to model the mechanical behavior of the Nomex® walls, [39–41]. The following equations summarize these criteria :

- Longitudinal failure in tension: $\sigma_{11} \geq 0$

$$e_l = \left(\frac{X_t}{\sigma_{11}}\right)^2 \quad \text{Eq. 6}$$

- Longitudinal failure in compression : $\sigma_{11} < 0$

$$e_l = \left(\frac{X_c}{\sigma_{11}}\right)^2 + \frac{1}{S_{12}}\left(\sigma_{12}^2 + \sigma_{13}^2\right) \quad \text{Eq. 7}$$

- Transverse failure in tension: $(\sigma_{22} + \sigma_{33}) \geq 0$

$$e_t = \frac{(\sigma_{22} + \sigma_{33})^2}{Y_t^2} + \frac{\sigma_{12}^2 + \sigma_{13}^2 + \sigma_{23}^2 - \sigma_{22}\sigma_{33}}{S_{12}^2} \quad \text{Eq. 8}$$

- Transverse failure in compression: $(\sigma_{22} + \sigma_{33}) < 0$

$$e_t = \frac{1}{Y_c}\left[\left(\frac{Y_c}{2S_{23}}\right)^2 - 1\right](\sigma_{22} + \sigma_{33}) + \frac{(\sigma_{22} + \sigma_{33})^2}{4S_{23}^2} \quad \text{Eq. 9}$$
$$+ \frac{\sigma_{23}^2 - \sigma_{22}\sigma_{33}}{S_{23}^2} + \frac{\sigma_{12}^2 + \sigma_{13}^2}{S_{12}^2}$$

2.4. Stiffness degradation concept in machining Nomex® and numerical scheme

The progressive failure analysis is a method of mechanical properties degradation of the material, in fact, the damaged elements are replaced by an equivalent material with degraded properties. There are several models in the literature that consider the material stiffness degradation, the most popular are: Total discount approach, limited discount method and residual property method [42–45]. In the last method, continuous damage models are used to predict progressive damage and stiffness drop in composite materials. Damage evolution laws are used to predict the accumulation of damage during the mechanical loading.

2.3.1. Tsai-Wu failure criterion

The Tsai-Wu criterion allows to identify the damage of each requested element when Eq. 1 is validated. however, it does not make it possible to identify the directions of damage of an element when damage criterion is verified. The direction is often needed to calculate and update the rigidity drop of elements. To overcome this difficulty, the Tsai-Wu criterion is separated into several stress components H_k ($k = 1$ to 6) in order to identify the modes and directions of the damage of elements (see Eq. 10), [38].

$$H_1 = F_1\sigma_1 + F_{11}\sigma_1^2$$
$$H_2 = F_2\sigma_2 + F_{22}\sigma_2^2 \quad \text{Eq. 10}$$
$$H_3 = F_3\sigma_3 + F_{33}\sigma_3^2$$
$$H_4 = F_{44}\sigma_{23}^2$$
$$H_5 = F_{55}\sigma_{12}^2$$
$$H_6 = F_{66}\sigma_{31}^2$$

More precisely, when the Tsai-Wu failure criterion is satisfied, the components H_k are calculated and compared with one another to identify the maximum value. The biggest term of H_k is then selected as the dominant mode of damage and the corresponding elastic modulus will undergo a decrease stiffness with degradation of the corresponding properties mentioned in Table 3. Thus, H_1 corresponds to a longitudinal rupture, H_2 to a transverse rupture, H_3 to a rupture in the thickness, H_4 to a shear failure 23, H_5 to a shear failure 12, and H_6 corresponds to a rupture 13, [38,46].

Table 3. Stiffness degradation and corresponding variables according to the Tsai-Wu criterion.

Elasticity Modules	Criterion of Tsai-Wu satisfied	
	Damage index	Degradation of mechanical properties
E_{11}	H_1	$E_{11} \rightarrow (1-d_1)\, E_{11}$
E_{22}	H_2	$E_{22} \rightarrow (1-d_2)\, E_{22}$
E_{33}	H_3	$E_{33} \rightarrow (1-d_3)\, E_{33}$
G_{23}	H_4	$G_{23} \rightarrow (1-d_4)\, G_{23}$
G_{12}	H_5	$G_{12} \rightarrow (1-d_5)\, G_{12}$
G_{13}	H_6	$G_{13} \rightarrow (1-d_6)\, G_{13}$

The damage model used in this study consists in reducing the stiffness on the different elasticity modules once the failure criterion is satisfied, see Table 3. The damage is characterized by several damage variables noticed di (i = 1 to 6) as shown by Eqs. 11 and 12. The expression of damage is an exponential function, Eq. 13, [47] :

$$E_{ij} = (1-d_k)E_{ij}^0 \quad \text{Eq. 11}$$
$$G_{ij} = (1-d_k)G_{ij}^0 \quad \text{Eq. 12}$$
$$d_k = 1 - exp\left[-\frac{1}{m\,e}\left(\frac{\varepsilon_{ij}}{\varepsilon_{fij}}\right)^m\right] \quad \text{Eq. 13}$$

The constant e is the number of Euler, m the constraint softening parameter taken equal to 10 to indicate brittle behavior. $\mathcal{E}_{fij}$ is the deformation of rupture in the axis according to which the damage is initiated, Eq. 14:

$$\varepsilon_{f11}=\frac{X_{t,c}}{E_{11}}\ ;\ \varepsilon_{f22}=\frac{Y_{t,c}}{E_{22}}\ ;\ \varepsilon_{f33}=\frac{Y_{t,c}}{E_{33}}\ ;\ \varepsilon_{f12}=\frac{S_{12}}{G_{12}}\ ;\ \varepsilon_{f13}=\varepsilon_{f23}=\frac{S_{13}}{G_{13}} \qquad \text{Eq.14}$$

with $X_{t,c}$ and $Y_{t,c}$ the limiting stresses of the material in the longitudinal and transverse directions, S_{ij} is the limit stress in shear, see Table 1.

2.3.2. Hashin failure criteria

Contrary to the Tsai-Wu criterion, Hashin criteria make it possible to further identify the modes and damage directions of each element satisfying the failure criterion. This identification allows to calculate and update the rigidity at each increment. Two indices of rupture are attributed to each element of the honeycomb walls, they represent the transversal damage and the longitudinal damage, Eqs. 6-9. Thus, as soon as an element satisfies Hashin criteria, it will undergo a decrease stiffness until his removal. Table 4 summarizes the mechanical properties to be degraded for each damage index verified by the Hashin criteria.

Table 4. Stiffness degradation and corresponding variables according to Hashin failure criteria.

No failure	Hashin failure criteria satisfied	
	Damage index	Degradation of mechanical properties
E_{11}	e_l	$E_{11} \rightarrow (1-d_1)\ E_{11}$
E_{22}	e_t	$E_{22} \rightarrow (1-d_2)\ E_{22}$
G_{23}	e_t	$G_{23} \rightarrow (1-d_3)\ G_{23}$
G_{12}	e_t	$G_{12} \rightarrow (1-d_4)\ G_{12}$

2.3.3. Analysis of the progressive damage procedure

The damage analysis procedure is illustrated in Figure 10. At the beginning of the analysis, the initial state of the material (Nomex® honeycomb) is undamaged, the initial mechanical properties of the material are those mentioned in Table 1. The advancement of the tool generates

a load which will be applied to the honeycomb part. The constraints are calculated at each Gauss integration point and used to evaluate the failure criteria described above. When the failure criterion (Tsai-Wu or Hashin) is checked, the variable assigned to it has the value 1, which means that at this stage of the simulation (calculation) the material is damaged. This variable is kept equal to this value for the rest of the calculation to consider the irreversibility of the damage process. The stiffness degradation is then made in the direction of damage, the direction is then determined according to the chosen rupture criterion. For the Hashin criterion, the damage direction is simply determined according to the verified criterion equation, for the case of the Tsai-Wu criterion, the damage direction is determined by the comparison of the different damage indices H_k. The specific stiffness degradation in the defined direction is applied as indicated in Tables 1 and 2. This procedure is repeated throughout the machining operation until the damage index d_i reaches the threshold limit of the stiffness degradation which causes the deletion of the concerned element. The removal of all damaged elements finally gives rise to the formation of the chip.

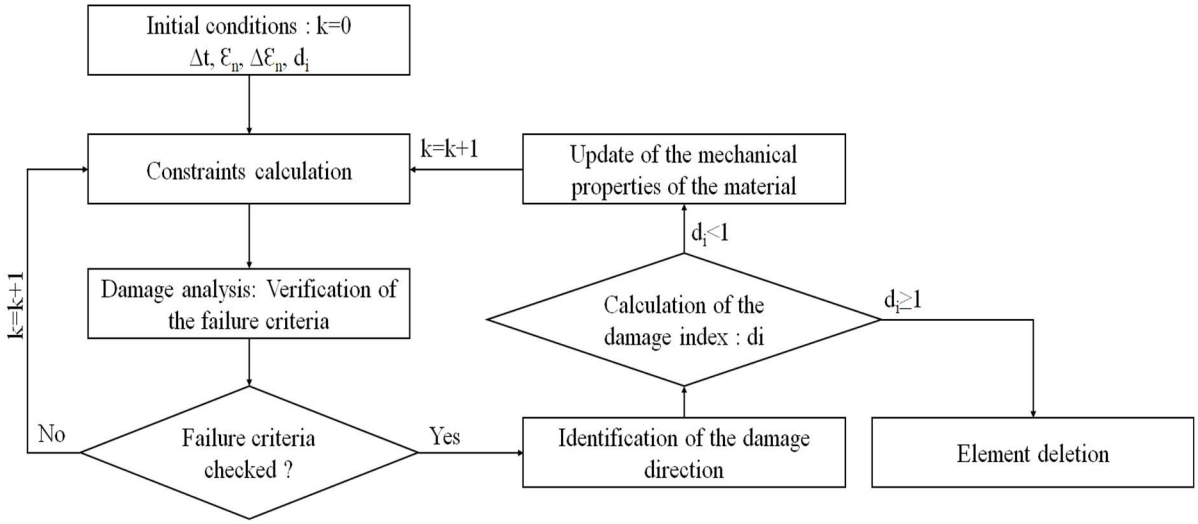


Figure 10. Algorithm for analysis of progressive damage induced in the walls of the Nomex® honeycomb.

3. Results and discussion

3.1. Analysis of the cutting forces

The three components of the cutting forces (*Fx*, *Fy* and *Fz*) in (X, Y, Z) directions (see Figure 7) are calculated and recorded in the reference point assigned to the tool. Figure 11 shows the evolution of these three components obtained for the cutting condition N= 10000 *rpm* and *f* =3000 mm/min as a function of time.

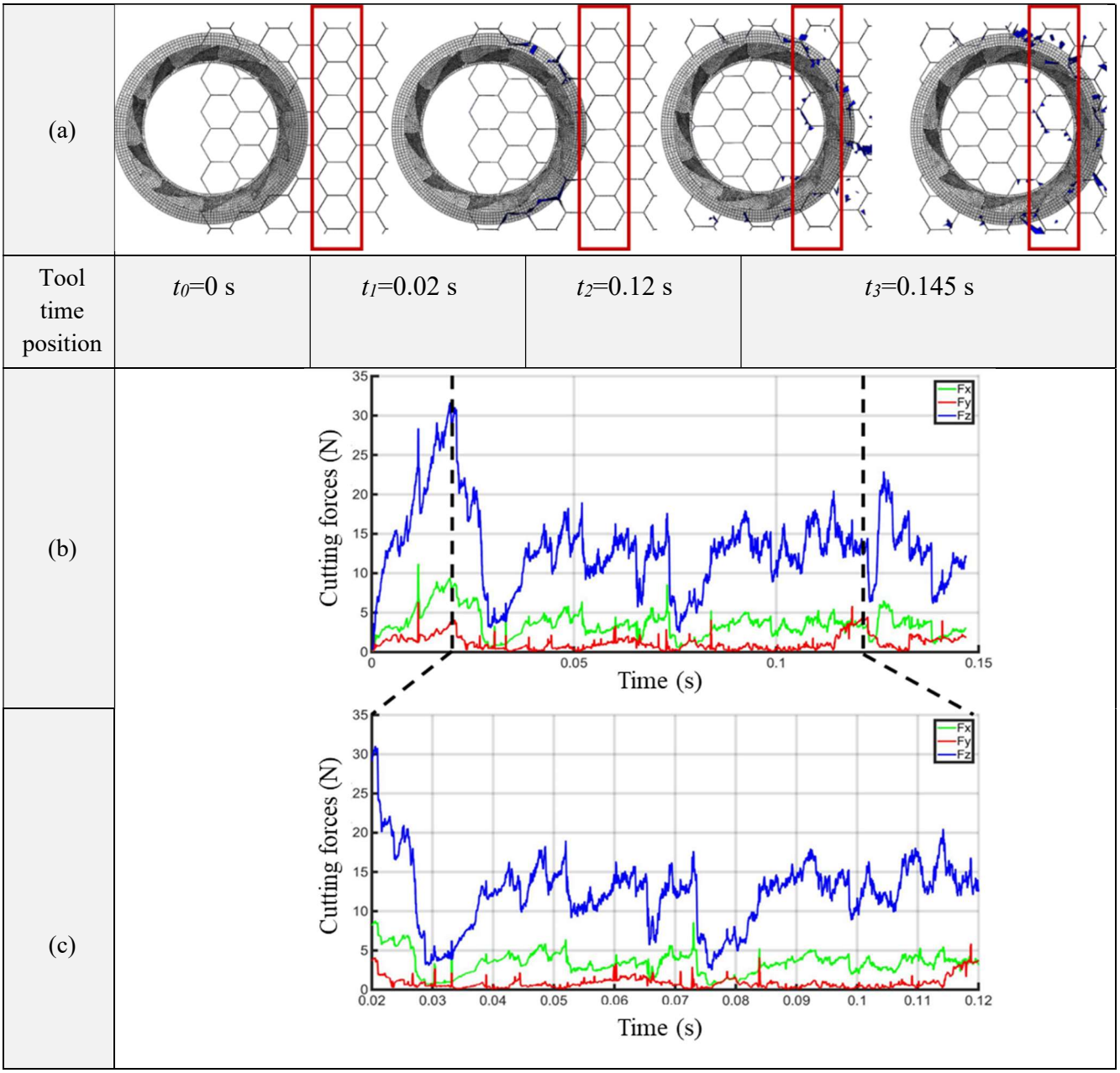


Figure 11. Evolution of the cutting force components (Fx, Fy and Fz) obtained by numerical simulation. The Tsai-Wu failure criterion was applied to the cutting condition: f=3000 mm/min and N=10000 tr/min. (a) Position time of the tool in the honeycomb workpiece during the milling operation. (b) Evolution of the cutting forces vs. machining time. (c) Zoom on the evolution of cutting forces for a single row of cells.

The cutting forces are calculated at each time increment during the movement of the cutting tool in the honeycomb workpiece. It is necessary to specify that the first row of cells that the tool encounters at the beginning of machining is not complete because we have reserved a location for the tool in the part (initial engagement of the tool) to reduce the calculation time, see Fig. 5(d). At time t=0s the tool is stopped. When it meets the first complete row of cells (in red rectangle of Fig. 11 (a)) it has already machined some cells before. It arrives at the beginning of the complete row at t=0.02s and finishes machining at about t=0.145s. The machining time of a complete row of cells (1 period) is therefore $t_{machining}$=0.145-0.02=0.125s. Figure 11 presents the evolution of the cutting forces vs. time with a feed rate of 3000mm/min which is twice that of Figure 12 (f=1500 mm/min). That is why the cutting time in Figure 12 (0.24s) is twice of that in Figure 11 (0.12s). Form this figure it can also be observed that the three components of the cutting force (*Fx*, *Fy* and *Fz*) increase continuously until t_1= 0.02s where the tool meets the first row of cells. Between t_1=0.02 s and t_2=0.12 s, the tool cut a row of honeycomb cells. Beyond t_2=0.12 s, the tool starts machining the next row. On the same curve, the temporary range used [t_1 t_2] is defined for the calculation of the average of cutting force components. For each cutting condition, only efforts generated to machine one row of cells are compared to the experimental results.

Figure 12 shows the evolution of the three predicted cutting force components (*Fx*, *Fy* and *Fz*) for the cutting condition N=15000 rpm and f=1500 mm/min obtained with the three approaches adopted in this study ((i)- simulation with elastoplastic and isotropic behavior, (ii)- simulation with orthotropic behavior using Tsai-Wu criterion and (iii)- ditto with Hashin criteria).

The evolution of cutting forces represents significant variations throughout the machining process. Variations of the order of 50% are observed on the cutting forces which characterize on one hand the formation of the chip and on the other hand the tool position: the forces are

greater when cutting the double walls, they decrease when cutting single walls. An increase in the cutting effort level is related to the cutting of double walls and junctions between the different walls, the tool encounters more amount of the material to be cut in these places. Variations in the order of 0.1N to 1N are observed on the cutting forces. These slight fluctuations accompany the evolution of the cutting forces, they are due to vibrations and friction effect between the walls of the honeycomb workpiece and the cutting tool.

Looking at the values of the cutting force components for the three simulations shown in Figure 12, we notice that the compression force *Fz* in blue color is more important than the other two components *Fx* and *Fy*, this is due to the mechanical behavior of the honeycomb structure which is characterized by a better resistance in the out-of-plane direction (O*z* direction) in comparison with the Ox and Oy directions, Figure 7(b).

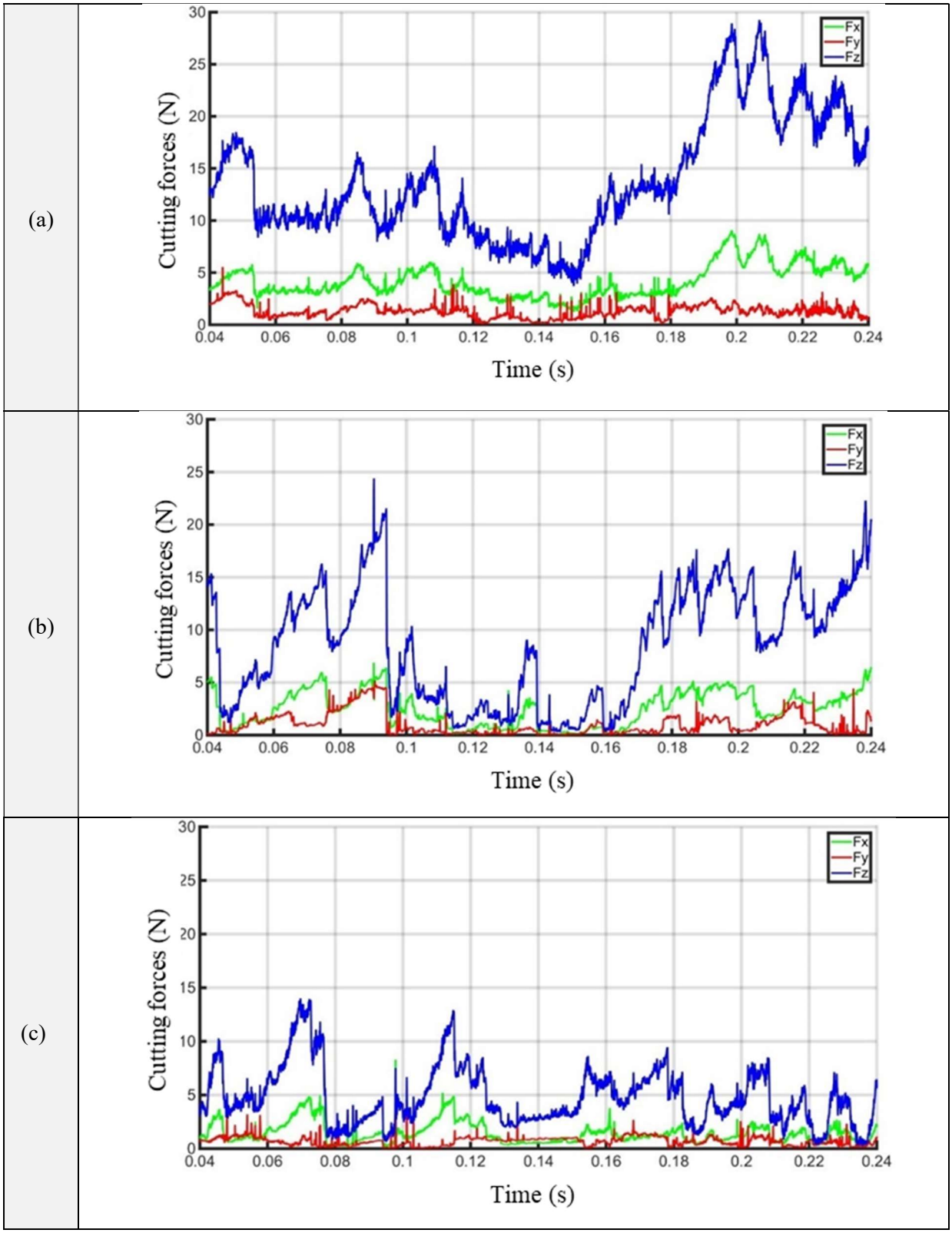


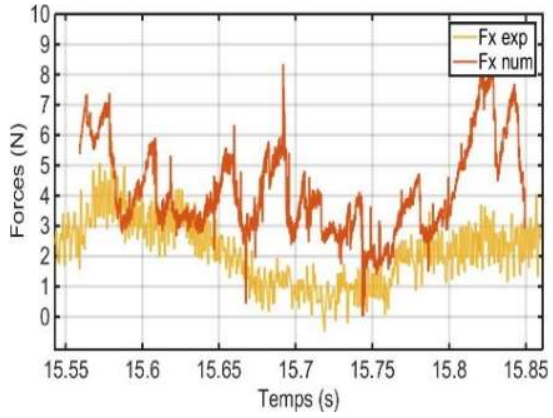
Figure 12. Evolution of the cutting force components (Fx, Fy and Fz) as a function of the machining time for the cutting condition f=1500mm/min and N= 15000 rpm. (a) Simulation with the isotropic elastoplastic model; (b) with the orthotropic model coupled to the Tsai-Wu failure criterion; (c) orthotropic model coupled to the Hashin criteria.

3.2. Comparison and experimental validation of the model

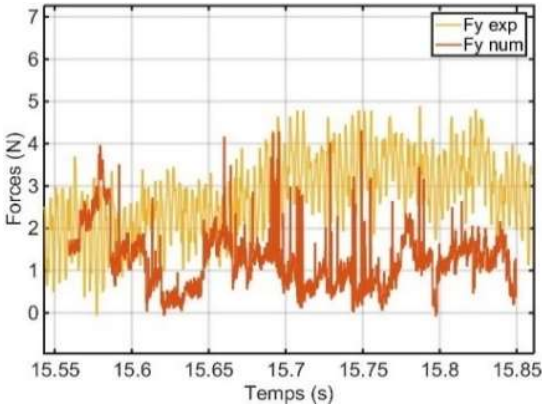
To validate the proposed model many experimental tests were performed in the current study. A detailed description of these machining tests is given in Subsection 2.2. The numerical simulations were performed on a row of cells. To be sure that at least one row of cells was cut, a minimum distance traveled by the tool of the order of 5 mm was considered.

Figures 13, 14 and 15 show a machining time of 0.3s which corresponds to the cutting time of a row of cells with a lower feed rate (1000mm/min). This explains the difference in machining time compared to Figure 11 (t=0.12s for f=3000 mm/min) and Figure 12 (t=0.24s for f=1500 mm/min).

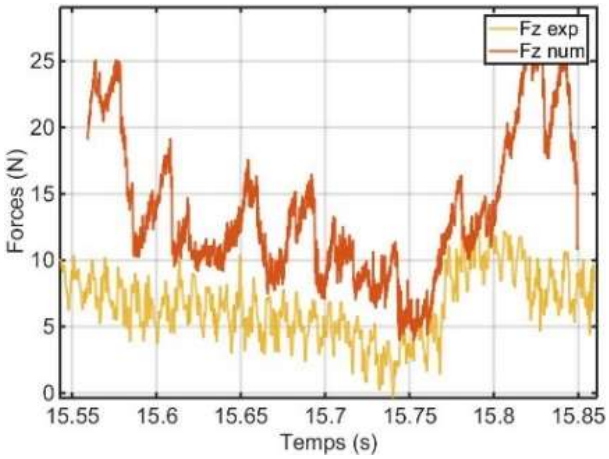
The cutting condition given by f = 1000 mm/min and N = 15000 rpm was used for both numerical simulations and experimental tests. The results are compared with those obtained experimentally.



(a)



(b)



(c)

Figure 13. Evolution of the cutting force components obtained for f=1000 mm/min, N=15000 rpm and ap=2mm with the isotropic elastoplastic approach: (a) Fx; (b) Fy; (c) Fz.

The experimental forces show some variations due to the alveolar geometry of the structure and to the vibrations coming from the thin walls of the cells of the honeycomb workpiece (the evolution of the experimental components of the cutting force is represented by a yellow line in Figures 13, 14 and 15). At the beginning of the machining process, the *Fx* and *Fz* forces show that the values decrease as the tool progresses in the workpiece material and then increase again. The two zones of significant effort correspond to the tool's contact with the double walls and junctions. This phenomenon is also reproduced by the forces predicted by numerical simulations.

The simulation with isotropic elastoplastic behavior gives a correct appearance of the evolution of the cutting efforts except that it overestimates them (Figures 13), this overestimation is more important at the input and output of the tool in the machined material. However, the Hashin failure criterion gives an underestimation of cutting forces (Figure 14). The simulation with the orthotropic behavior and the Tsai-Wu failure criteria offers a better correlation with the evolution of the experimental efforts in comparison with the other approaches, (Figure 15).

These remarks are valid for all components (*Fx* and *Fz*) except *Fy*, the three simulations showed an underestimation of this component compared to the experimental evolution. The force *Fy* does not generally exceed 1N and often remains almost zero as it can be observed for the case of the simulation with the Hashin criterion, Figure 14-b. One can say that the numerical results are in good agreement with those obtained experimentally except for the tangential force *Fy*. It was concluded from this study that whatever the chosen failure criteria (Hashin or Tsai-Wu) or cutting conditions, the tangential force *Fy* remains all the time low in comparison with experiments. These low values can be explained by the suppression elements procedure generated by the failure criterion under Lagrangian formulation in Abaqus code. The element

suppression leads to the contact loss between the cutting blade and honeycomb cells, and then the loss of the local rigidity.

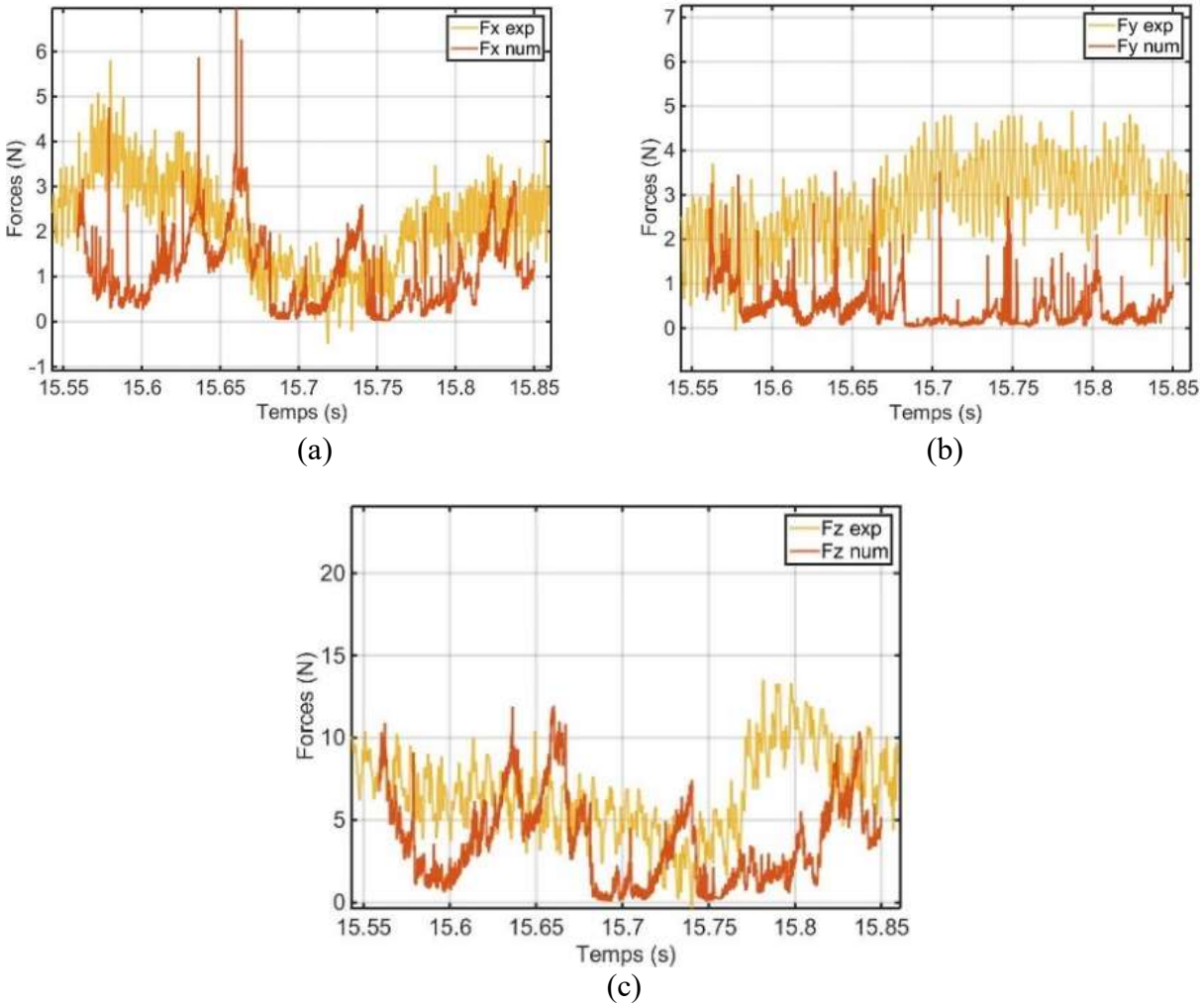
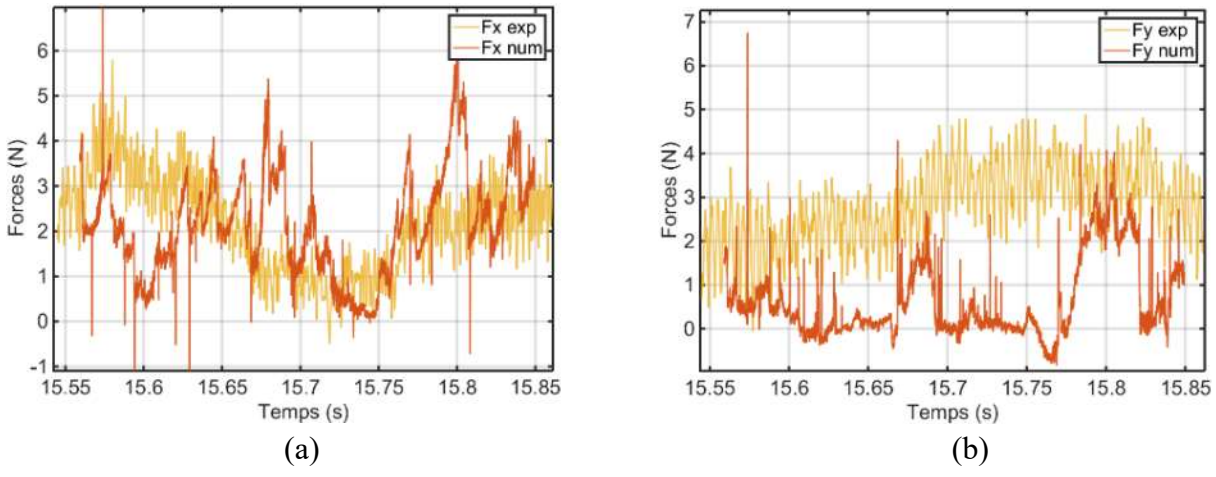
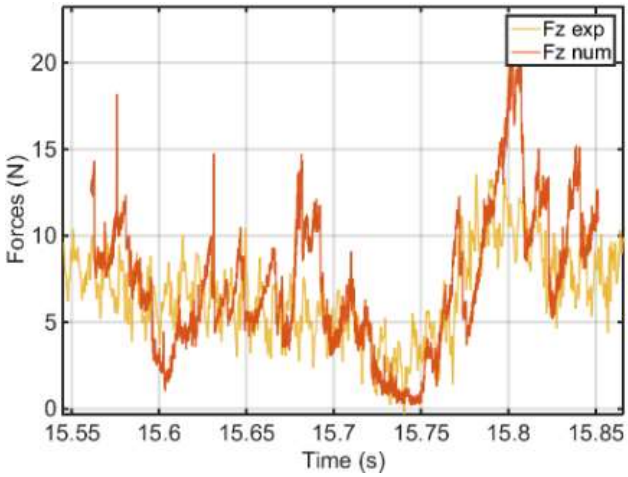


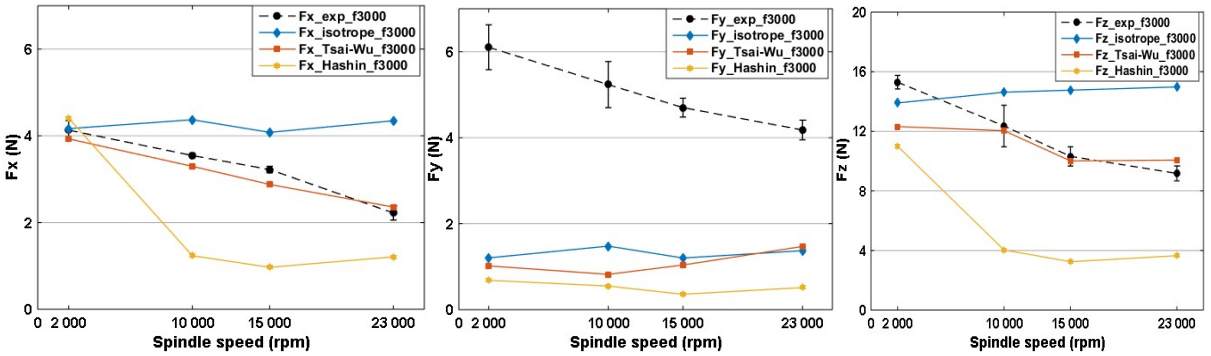
Figure 14. Evolution of the cutting force components obtained with the monolayer orthotropic approach and Hashin failure criteria, the selected cutting condition is : f=1000 mm/min, N=15000 tr/min and ap=2mm: (a) Fx; (b) Fy; (c) Fz.



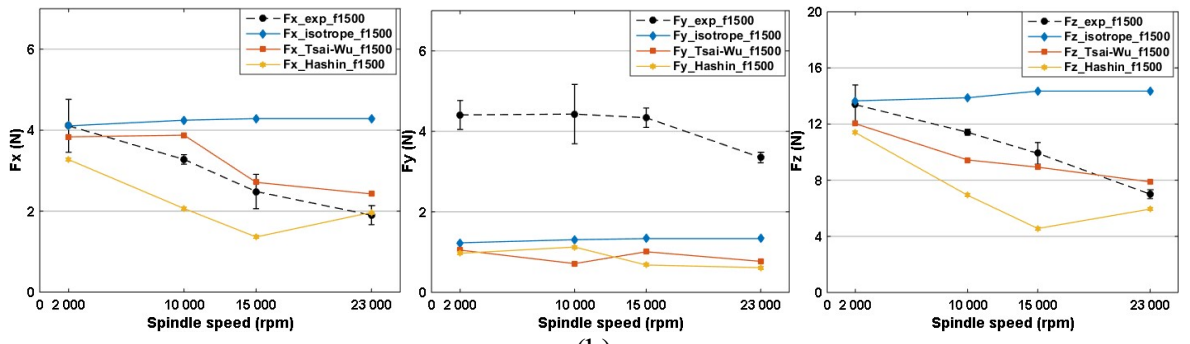


(c)

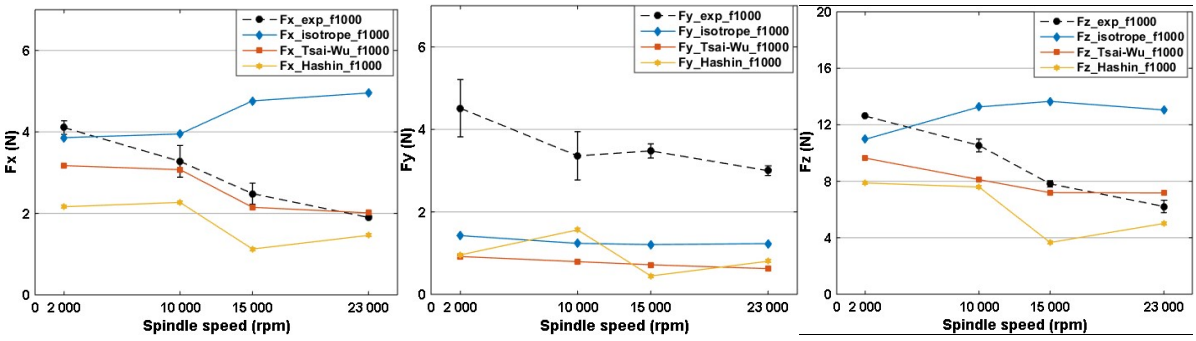
Figure 15. Evolution of the cutting force components obtained with the orthotropic approach and Tsai-Wu failure criterion, the used cutting condition is: f=1000 mm/min, N=15000 rpm and ap=2mm: (a) Fx; (b) Fy; (c) Fz.



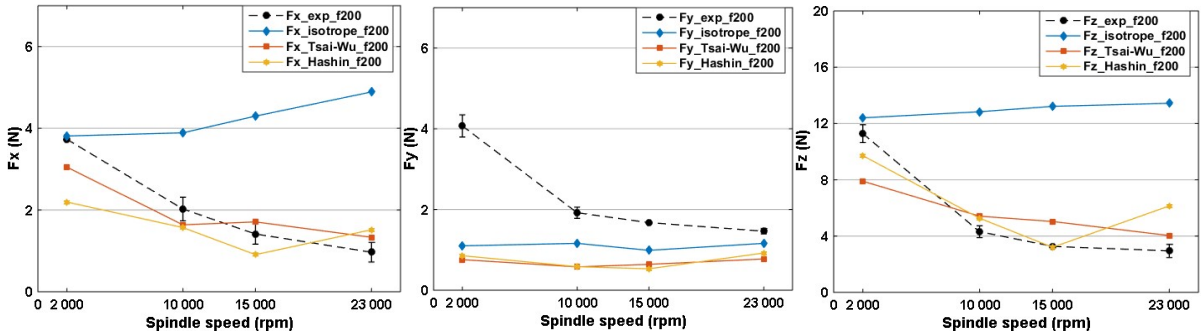
(a)



(b)



(c)



(d)

Figure 16. Evolution of the cutting force components (Fx, Fy and Fz) vs. the cutting speed N for the three numerical simulations: (i)- monolayer isotropic approach, (ii)- monolayer orthotropic approach with Tsai-Wu failure criterion, and (iii)- monolayer orthotropic approach with Hashin failure criteria. (a) corresponds to tests with f = 3000 mm/min; (b) f = 1500 mm/min; (c) f = 1000 mm/min; (d) f = 200 mm/min.

The average values of the different numerically predicted components of the cutting force and those measured experimentally were determined. Figure 16 presents a comparison between each component of the cutting force obtained by the three different simulations: (i)- monolayer isotropic approach, (ii)- monolayer orthotropic approach with Tsai-Wu failure criterion, and (iii)- monolayer orthotropic approach with Hashin failure criteria. Different cutting conditions were tested: (a) f = 3000 mm/min; (b) f = 1500 mm/min; (c) f = 1000 mm/min; (d) f = 200 mm/min. The measurements of the different components of the cutting force (*Fx*, *Fy* and *Fz*) show experimentally a decrease function of the spindle speed *N* and an increase function with the feed rate *f*. The compressive force *Fz* is the most important effort when cutting the Nomex® honeycomb structures.

At first sight, the force *Fy* predicted by the three simulations shows a gap with experimental data, a significant difference can be observed between the experimental and numerical value for all tested cutting conditions (see Figures 16 (a), (b), (c) and (d)). This disagreement between the numerical model and experiments can easily be explained by the lack of the spring-back of walls on the tool flank surface. This phenomenon is well known when using finites elements numerical simulation with the Lagrangian formulation [43]. Thus, when the element reaches

the mechanical rupture threshold, it is deleted. This deletion is accompanied by a loss of contact between the material and the cutting tool which depresses the cutting efforts, [44]. Indeed, springback uncut walls leads to resistance following the opposite direction of rotation of the tool and therefore generates increased cutting force. For any cutting condition, the force *Fy* remains constant and does not exceed the value of 2N while the experimental value is around 3N or 4N.

By observing the evolution of the cutting force components as a function of the feed rate *f* and the spindle speed *N*, the isotropic elastoplastic model clearly shows a behavior opposite to that generally known for composite materials, with an increase in the cutting force level with the spindle speed for the four selected feed rates. The plastic deformation attributed to this model is likely to be the source of this behavior, this deformation delays the removal of the elements which causes an accumulation of the material in front of the tool and leads to increased cutting efforts. This allows an overestimated value for the machined material resistance. This overestimation of the cutting forces is more and more important when increasing the cutting speed *N*. It can be concluded that the simulation with the isotropic elastoplastic behavior is not adapted to the machining operation even if it represents the behavior of the off-plane compression structure, [32,50,51].

Otherwise, the simulation with the approach based on the orthotropic behavior with the Hashin failure criteria has similar results to that obtained by experimental tests with generally a decrease in cutting forces when the cutting speed (spindle speed) increases. The calculated cutting forces are generally lower than those observed experimentally. The higher the feed rate is, the greater is the underestimation and can reaches 3 times the value observed experimentally. The Hashin failure criteria is more efficient at low feed rate (f = 200 mm / min), Figure 16 (d). Thus, these failure criteria give the good results at very high spindle speeds and improve even more with the decrease of the feed rate (case of the chip fragmentation).

In the case of the Tsai-Wu failure criterion, it can be noticed that some efforts calculated by the numerical simulation seem to correlate with the experimental data except for the effort *Fy*. This criterion shows an analogy with that of Hashin, with a slight underestimation for the high spindle speed 23000 rpm and an underestimation for low speeds. However, overall it gives a good estimation.

The differences obtained by comparing the experimental results and those of the numerical simulation show that the three simulations fail to reproduce the evolution of the tangential effort *Fy*. The latter is determined with an average difference greater than 60% for the three used simulations. As said before, the origin of this discrepancy is explained by most authors as being due on one hand to the elastic bouncing-back of the material and on the other hand, to the hypothesis of homogenization of the honeycomb wall behavior.

For the other components of the cutting force, the two rupture criteria (Hashin, Tsai-Wu) show similar results to those observed in the experimental trends, with a decrease in the effort level with increasing the cutting speed or spindle speed.

Finally, it can be said that the Tsai-Wu criterion is that which gives a better trend compared to other simulations and especially for the compression force *Fz* which represents the component of the largest cutting force.

3.3. *Chip formation*

The difference in diameter between the saw blade and the upper part of the cutting tool (shredder) makes the cutting process of walls very complicated (the difference in diameters is about 2.2 mm between the cutting blade and the shredder, see Figure 3(b)). This causes the chip formation in several steps. The saw blade is the first component of the tool that meets the honeycomb walls. Figure 17 shows the different stages of the honeycomb milling operation and

the chip formation process for the condition : f = 3000 mm / min and N = 2000 rpm. The simulations was done with the Tsai-wu failure criterion and shown in Figures 17 and 18.

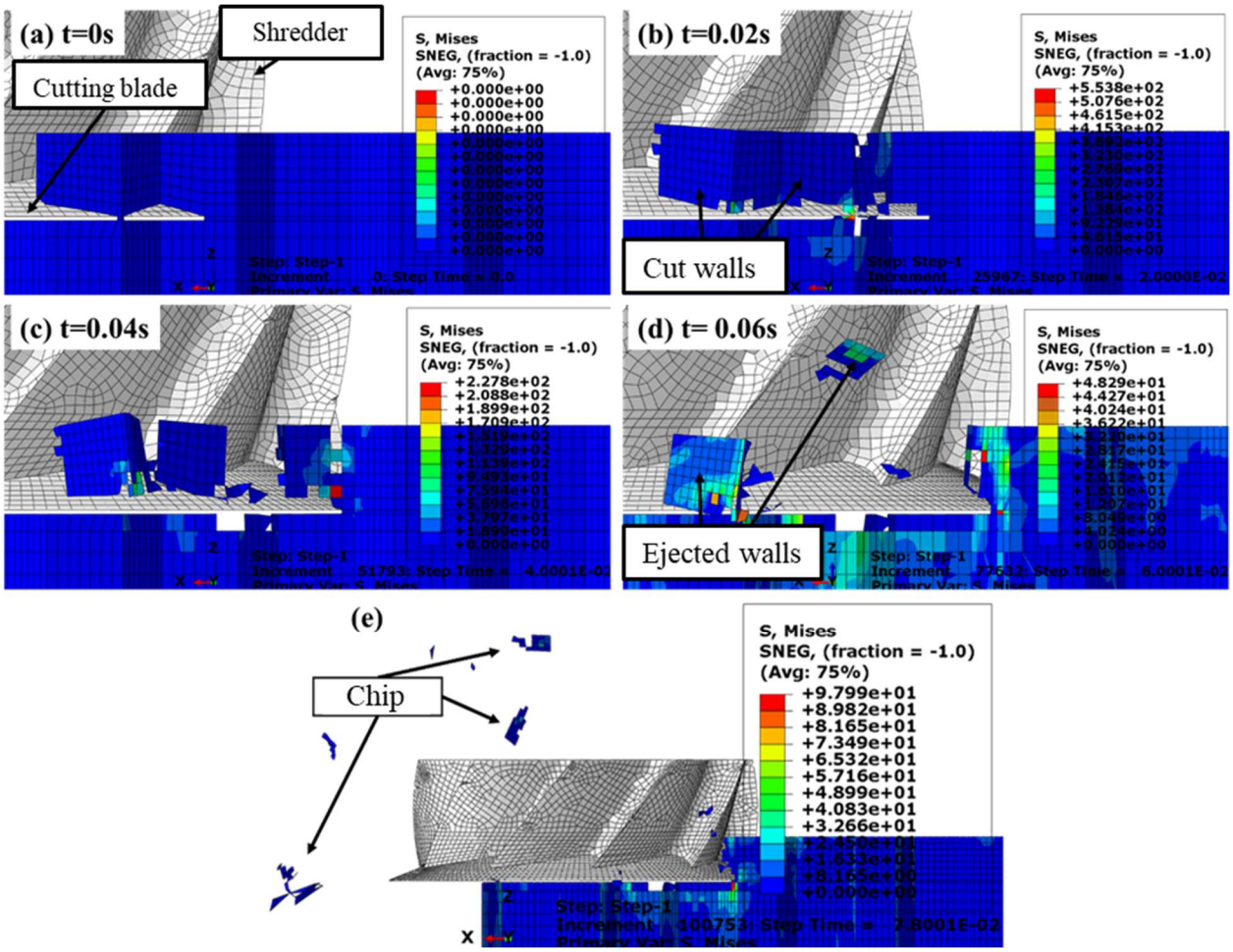


Figure 17. Simulation of the milling process on the Nomex® structure for f = 3000 mm / min and N= 2000 rpm with the use of the Tsai-Wu failure criterion. Different steps of the chip formation process are presented: (a) t=0s; (b) t=0.02s; (c) t=0.04s; (d) t=0.06s; (e) generation of fragmented chips.

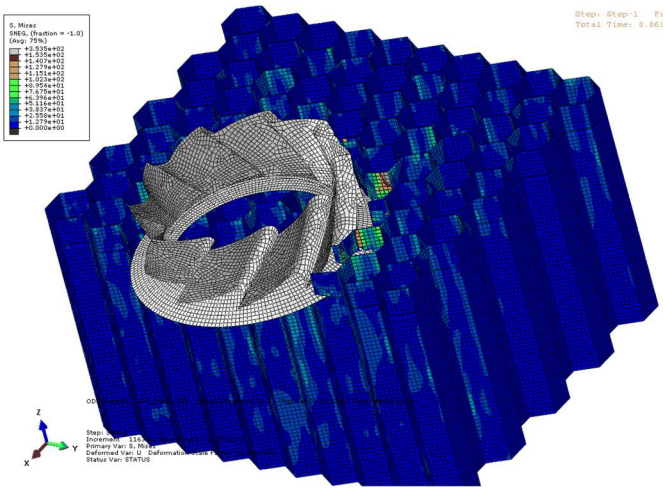


Figure 18. Distribution of stress on the honeycomb walls during machining. Cutting condition: f=3000 mm/min and N=2000 rpm.

The first element of the tool that will be in contact with the honeycomb walls is the saw blade. This element starts with cutting the walls by turning and advancing in the material. Thus, the cutting and the separation of walls occur by damage and friction processes. The advancement and rotation of the tool make the stresses very high in the elements of the walls, see Figure 18.

At each increment, the failure criteria are checked, if they are satisfied the damaged elements are removed to form the chip (Figures 17 (a) and (b)). This stage represents the first phase of the chip formation that will be generated from the walls previously cut by the cutting blade but which remains always attached to the structure. The chip is not completely formed at this stage of the process. In the next step, the detached walls of the structure flow on the upper face of the saw blade until reaching the shredder. Thus, the shredder through these 10 propellers and chip brakers cut these walls into several slices, this upper part of the tool has the role of shredding the walls and thus release the passage to the tool to advance in the material. At this stage, the chip is completely formed. Moreover, the walls cut by the saw blade encounter the upper part of the tool and other neighboring walls which will deform while remaining attached to the structure until the satisfaction of the failure criterion, (Figure 17 (c) and (d)). These walls will then be pushed back and ejected by the upper part of the tool (Figure 17(e)) forming other chips. These different cutting steps were observed for the three types of simulations. These mechanisms of the chip formation process are intrinsically related to the geometry of the honeycomb structure and that of the cutting tool.

The steps of the Nomex® cutting previously described are verified experimentally. With the high-speed camera, the interaction zone between the Nomex® and the cutting tool was observed. Figure 19 shows the different cutting steps of the Nomex® walls. The latter are firstly cut by the saw blade, the cut walls remain attached to the structure and slides on the upper surface of the saw blade until reaching the shredder, then, the shredder pushes or cuts them in small chips according to the spindle speed or cutting speed.

The total formation of the chip is done once the walls cut beforehand by the saw blade are shredded and pushed back by the upper part of the tool. The upper surface of the saw blade represents the cutting face, and the lower surface represents the flank face since it is in contact with the freshly machined material. The action of the two tool parts prevents the cut material wraps around the tool which can damage the workpiece or even drag it outside the machine table.

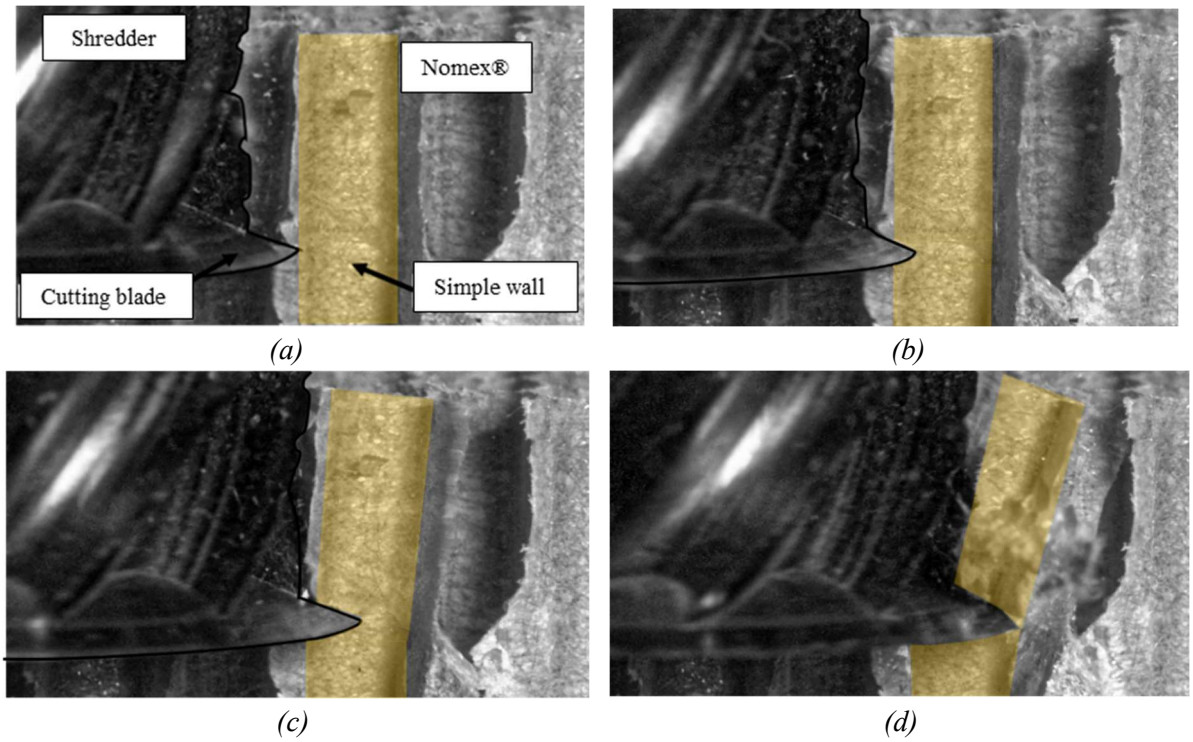


Figure 19. Mechanisms of the chip formation process during machining Nomex®, the selected cutting condition is: f=1000 mm/min and N=15000 rpm.

Figure 20 shows the accumulation of material (cell walls) at the front of the cutting tool upper part for two machining condition combinations (f = 3000 mm / min, N = 2000 rpm) and (f = 200 mm / min, N = 2000 rpm). This accumulation depends on the ability of the upper part of the tool to cut the honeycomb walls and evacuate them far from the cutting area.

The accumulation of material in front of the shredder depends on the machining conditions, it is more important for high feed rates and low spindle speeds (Figure 20(a)). The low spindle speed forces the shredder to push back the walls and not to cut them properly, with a high feed

rate, the amount of the removed material is greater which generates chips formed by several walls.

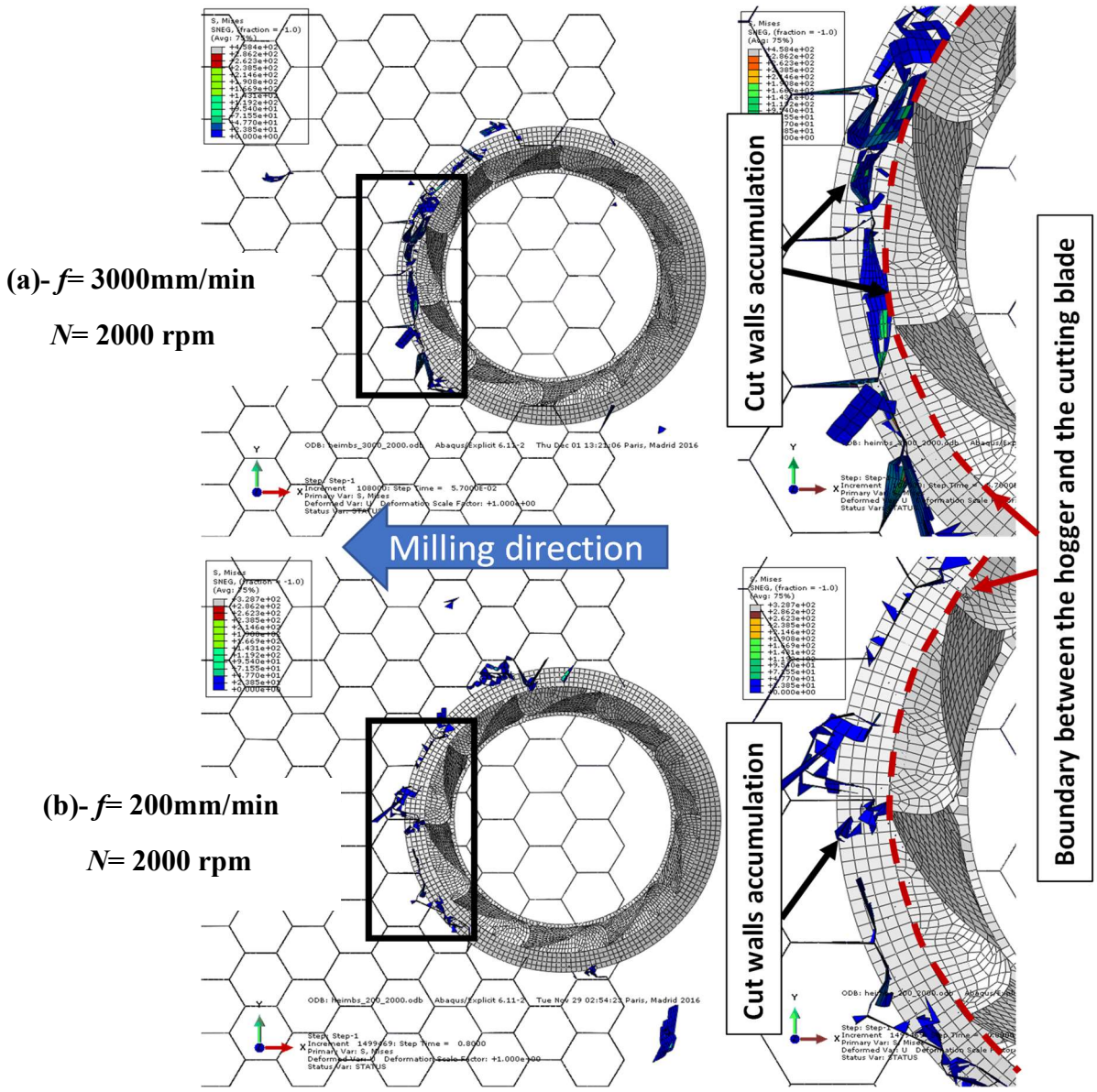


Figure 20. Accumulation of the cell walls at the front of the tool, the cutting conditions are: (a) f= 3000 mm/min and N= 2000 rpm, (b) f= 200 mm/min and N= 2000 rpm.

For low feed rates, there is an almost negligible accumulation of material in front of the shredder (Figure 20 (b)). In fact, the walls cut by the saw blade rub on the upper surface until reaching the shredder, they are then quickly shredded by the upper part of the tool. This is explained by the low feed rate which means that the amount of material removed by the tool for a single pass is very small and therefore the chips generated are of very small sizes (dust chips).

As shown in Figure 21, these results are in good agreement with observations made during the experimental study which showed that : (i)- for high feed rates (f=3000mm) and low spindle speeds (N=2000rpm), the chip is composed of a set of honeycomb walls Figures 21(a) and (b), and (ii)- for low feed rates (f=200mm) and high spindle speeds (N= 23000 rpm), chips morphologies are formed with very small sizes as dust chips (Figures 21(c) and (d)).

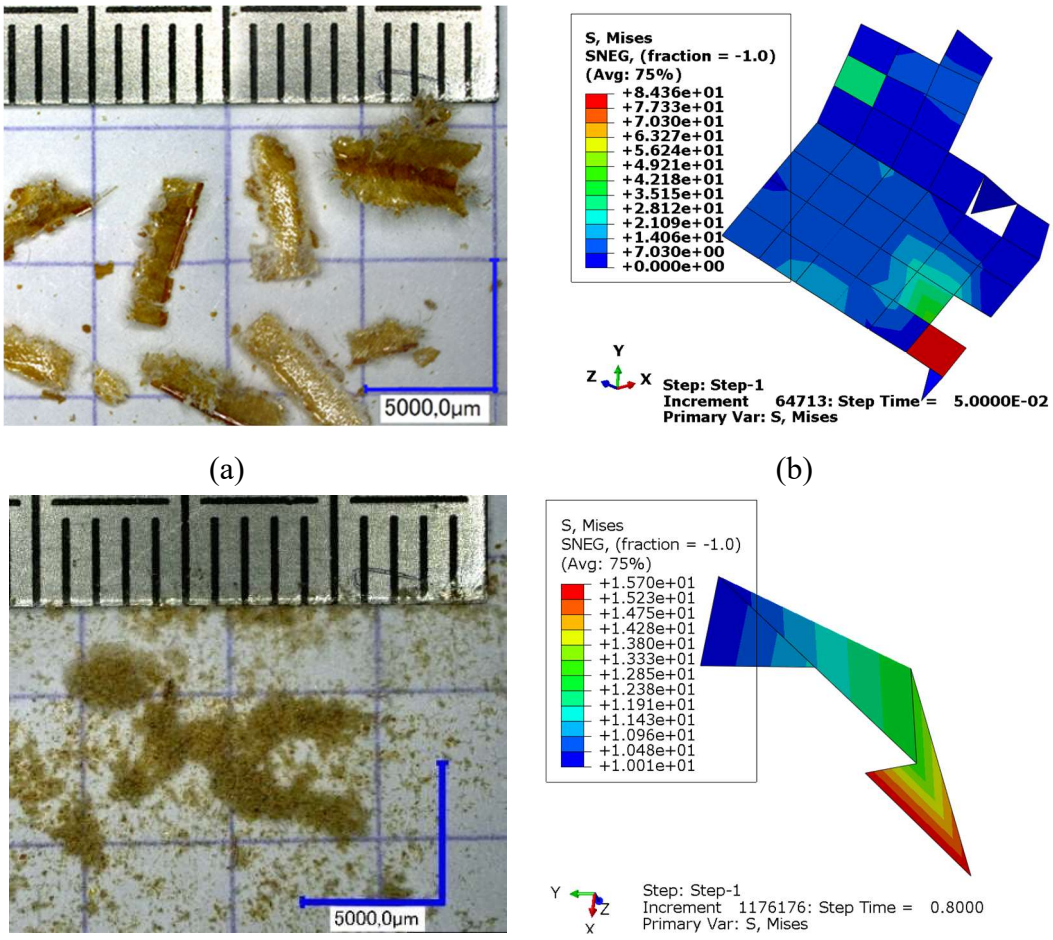


Figure 21. Different morphologies of the chip observed and simulated during machining of Nomex® honeycomb material. (a) Experimental chips made from the whole Nomex® cell walls, and (b)- simulated chips for the cutting condition: f= 3000 mm/min et N= 2000 tr/min. (c) and (d) experimental and simulated dust chips formed at f= 200 mm/min et N= 23000 rpm.

4. Conclusion

Honeycomb structures are characterized by their alveolar shape and complex geometry which make the numerical simulation of the behavior of this type of material complicated. Generally,

the structure is homogenized to simplify its behavior influenced by the different geometrical and physical parameters. The challenge of numerical modeling of the honeycomb cut concerns the 3D representation of the milling operation with a cutting tool having a complex geometry (industrial tools).

Three types of simulations were performed. Firstly, an isotropic elastoplastic behavior was attributed to the walls of Nomex®, in a second time, an orthotropic behavior with the Hashin failure criteria was used, and finally the Tsai- Wu failure criterion was associated with the orthotropic behavior of the honeycomb walls. The different stages of honeycomb wall cutting process have been analyzed and the physical mechanisms of the chip formation process have been accurately described. In addition, the proposed models predicted the cutting effort components and morphologies of chips with a good agreement comparing to the experimental tests. The proposed models also make it possible to study the effect of cutting parameters on the behavior of honeycomb structures.

The following conclusions can be drawn:

- Among the three proposed numerical approaches for machining Nomex®, the orthotropic approach with using the Tsai-Wu failure criterion showed a better prediction of honeycomb cutting. Nomex® paper is made of short fibers which has favored the Tsai-Wu criterion over that of Hashin criteria.

- The isotropic elastoplastic approach is not suitable for modeling the cut of the Nomex® honeycomb, it shows a different behavior from that observed in the experimental tests, the cutting forces increase with the increase in the spindle speed level.

- Machining Nomex® is characterized by the generation of low cutting forces that do not exceed 25N, the use of the monolayer orthotropic modeling associated to the Tsai-Wu

criterion makes possible the prediction of cutting forces. The latter are characterized by variations due to vibration of the structure and friction between walls and cutting tool.

- The cutting forces increase at the meeting of the double walls and junctions of cells since more material it removed. The reproduction of the *Fy* cutting effort remains limited due to absence of the well-known 'spring-back effect' because of the element suppression.

5. Declarations

Authors' contributions

M. JAAFAR obtained his PhD from LEM3 Laboratory at Lorraine University and performed in this work the literature study of this area of research and performed the model for numerical simulations. He also participated to writing the paper.

NOUARI is a full professor and the first supervisor of the work. He provided fundamental ideas and all needed support conditions. M. NOUARI organized the proof reading and critical revisions.

H. MAKICH is currently an associate professor and the second supervisor of this thesis project. He was in charge the experimental validation of the model. All authors read and approved the final manuscript.

M. MOUFKI is a full professor, his contribution to the work concerns the preparation of simulations. He also participates to the organization of the proof reading and critical revisions

All authors participated to read and approve the final manuscript.

Funding

No funding was obtained for this work except the salary of the PhD student given by the French Ministry of high education and research.

Data availability

All numerical data presented in this paper are available.

Compliance with ethical standards

Competing interests

The authors declare no competing financial interests.

Ethical approval

All ethical responsibilities were respected by the authors.

Consent to participate

All authors contribute and participate to work carried out in article.

Consent to publish

The authors of this paper agree to publish the results of this work carried out in the thesis of M. Jaafar.

Acknowledgments

The authors wish to express their thanks and appreciation to members of the following organizations for their financial support: Evatec-tools group and National French Research Agency (ANR). LARIOPAC Labcom project under Grant No. ANR-13-LAB2-0002.

References

[1] Lamb AJ. (2007) Experimental investigation and numerical modelling of composite-honeycomb materials used in Formula 1 crash structures. Dissertation, Cranfield University. https://doi.org/10.1017/CBO9781107415324.004.

[2] Fischer S, Drechsler K, Kilchert S, Johnson A. (2009) Mechanical tests for foldcore base material properties. Compos Part A 40:1941–52.

https://doi.org/10.1016/j.compositesa.

[3] Foo CC, Chai GB, Seah LK. (2007) Mechanical properties of Nomex material and Nomex honeycomb structure. Compos Struct 80:588–94. https://doi.org/10.1016/j.compstruct.2006.07.010.

[4] Kim DS, Lee JR. (1997) Compressive mechanical properties of the nomex/thermoset honeycomb cores. Polym Adv Technol 8:1–7. https://doi.org/10.1002/(SICI)1099-1581(199701)8:1<1::AID-PAT601>3.0.CO;2-G.

[5] Zinno A, Prota A, Di Maio E, Bakis CE. (2011) Experimental characterization of phenolic-impregnated honeycomb sandwich structures for transportation vehicles. Compos Struct 93:2910–24. https://doi.org/10.1016/j.compstruct.2011.05.012.

[6] Aminanda Y, Castanie B, Barrau JJ, Thevenet P. (2009)Experimental and numerical study of compression after impact of sandwich structures with metallic skins. Compos Sci Technol 69:50–9. https://doi.org/10.1016/j.compscitech.2007.10.045.

[7] Heimbs S. (2008) Sandwichstrukturen mit Wabenkern: Experimentelle und numerische Analyse des Schädigungsverhaltens unter statischer und kurzzeitdynamischer Belastung. Institut für Verbundwerkstoffe GmbH.

[8] Hou B, Ono A, Abdennadher S, Pattofatto S, Li YL, Zhao H. (2011) Impact behavior of honeycombs under combined shear-compression. Part I: Experiments. Int J Solids Struct 48:698–705. https://doi.org/10.1016/j.ijsolstr.2010.11.005.

[9] Mohr D, Doyoyo M. (2004) Deformation-induced folding systems in thin-walled monolithic hexagonal metallic honeycomb. Int J Solids Struct 41:3353–77. https://doi.org/10.1016/j.ijsolstr.2004.01.014.

[10] Wang, Z., Qin, Q., Chen, S., Yu, X., Li, H., Wang, T. J. (2017). Compressive crushing of novel aluminum hexagonal honeycombs with perforations: Experimental and numerical investigations. International Journal of Solids and Structures, 126, 187-195. https://doi.org/10.1016/j.ijsolstr.2017.08.005.

[11] Keshavanarayana, S. R., Shahverdi, H., Kothare, A., Yang, C., Bingenheimer, J. (2017). The effect of node bond adhesive fillet on uniaxial in-plane responses of hexagonal honeycomb core. Composite Structures, 175, 111-122. https://doi.org/10.1016/j.compstruct.2017.05.010.

[12] Zhang, Z. J., Han, B., Zhang, Q. C., Jin, F. (2017). Free vibration analysis of sandwich beams with honeycomb-corrugation hybrid cores. Composite Structures, 171, 335-344. https://doi.org/10.1016/j.compstruct.2017.03.045.

[13] Nasution, M. R. E., Watanabe, N., Kondo, A. (2015). Numerical study on thermal buckling of CFRP–Al honeycomb sandwich composites based on homogenization–localization analysis. Composite Structures, 132, 709-719. https://doi.org/10.1016/j.compstruct.2015.06.009.

[14] Lhuissier P, Laszczyk L. (2012) Caractérisation des structures sandwich. Tech l'Ingénieur, Ref : M5815 v1

[15] Hosseini, S. M. H., Gabbert, U. (2013). Numerical simulation of the Lamb wave propagation in honeycomb sandwich panels: a parametric study. Composite Structures, 97, 189-201. https://doi.org/10.1016/j.compstruct.2012.09.055.

[16] Manet, V. (2012). The use of Ansys to calculate sandwich structures. arXiv preprint arXiv:1201.5561. https://doi.org/DOI: 10.1016/S0266-3538(98)00010-4.

[17] Bianchi, G., Aglietti, G. S., Richardson, G. (2012). Static and fatigue behaviour of hexagonal honeycomb cores under in-plane shear loads. Applied Composite Materials, 19(2), 97-115. https://doi.org/10.1007/s10443-010-9184-5.

[18] Foo, C. C., Chai, G. B., Seah, L. K. (2008). A model to predict low-velocity impact response and damage in sandwich composites. Composites Science and Technology, 68(6), 1348-1356. https://doi.org/10.1016/j.compscitech.2007.12.007.

[19] Mancha, Á. J. (2012). Optimization of lightweight sandwich structures of commercial aircraft interior parts subjected to low-velocity impact. Universidad Pontificia Comillas Madrid, Escuela Tecnica Superior de Ingenierla (ICAI).

[20] Iváñez del Pozo, I., Moure Cuadrado, M. M., García Castillo, S. K., Sánchez Sáez, S. (2015). The oblique impact response of composite sandwich plates. https://doi.org/10.1016/j.compstruct.2015.08.035.

[21] Zhu, S., Chai, G. B. (2013). Damage and failure mode maps of composite sandwich panel subjected to quasi-static indentation and low velocity impact. Composite structures, 101, 204-214. https://doi.org/10.1016/j.compstruct.2013.02.010.

[22] Roy, R., Kweon, J. H., Choi, J. H. (2014). Meso-scale finite element modeling of NomexTM honeycomb cores. Advanced Composite Materials, 23(1), 17-29. https://doi.org/10.1080/09243046.2013.862382.

[23] Seemann, R., Krause, D. (2017). Numerical modelling of Nomex honeycomb sandwich cores at meso-scale level. Composite Structures, 159, 702-718. https://doi.org/10.1016/j.compstruct.2016.09.071.

[24] Roy, R., Park, S. J., Kweon, J. H., Choi, J. H. (2014). Characterization of Nomex honeycomb core constituent material mechanical properties. Composite Structures, 117, 255-266. https://doi.org/10.1016/j.compstruct.2014.06.033.

[25] Heimbs, S. (2009). Virtual testing of sandwich core structures using dynamic finite element simulations. Computational Materials Science, 45(2), 205-216. https://doi.org/10.1016/j.commatsci.2008.09.017.

[26] Roy, R., Nguyen, K. H., Park, Y. B., Kweon, J. H., Choi, J. H. (2014). Testing and modeling of Nomex™ honeycomb sandwich Panels with bolt insert. Composites Part B: Engineering, 56, 762-769. https://doi.org/10.1016/j.compositesb.2013.09.006.

[27] Kilchert, S. (2013). Nonlinear finite element modelling of degradation and failure in folded core composite sandwich structures. Dissertation, Faculty of Aerospace Engineering and Geodesy of the Universität Stuttgart.

[28] Seemann, R. A. L. F., Krause, D. I. E. T. E. R. (2014, July). Numerical modelling of nomex honeycomb cores for detailed analyses of sandwich panel joints. In 11th World Congress on Computational Mechanics (WCCM XI).

[29] Asprone, D., Auricchio, F., Menna, C., Morganti, S., Prota, A., Reali, A. (2013). Statistical finite element analysis of the buckling behavior of honeycomb structures. Composite Structures, 105, 240-255. https://doi.org/10.1016/j.compstruct.2013.05.014.

[30] Gornet, L., Marguet, S., Marckmann, G. (2007). Modeling of Nomex® honeycomb cores, linear and nonlinear behaviors. Mechanics of advanced Materials and structures, 14(8), 589-601. https://doi.org/10.1080/15376490701675370.

[31] Hähnel, F., Wolf, K. (2008). Simulation of the damage tolerance behaviour of CFRP/Honeycomb sandwich based on measured properties of the resin impregnated core paper. In Proc. of the 13th International Conference on Composite Materials, Stockholm. https://doi.org/10.1007/978-3-540-79432-5.

[32] Aktay, L., Johnson, A. F., Kröplin, B. H. (2008). Numerical modelling of honeycomb core crush behaviour. Engineering Fracture Mechanics, 75(9), 2616-2630. https://doi.org/10.1016/j.engfracmech.2007.03.008.

[33] Giglio, M., Manes, A., Gilioli, A. (2012). Investigations on sandwich core properties through an experimental–numerical approach. Composites Part B: Engineering, 43(2), 361-374. https://doi.org/10.1016/j.compositesb.2011.08.016.

[34] Qiu, K., Ming, W., Shen, L., An, Q., Chen, M. (2017). Study on the cutting force in machining of aluminum honeycomb core material. Composite Structures, 164, 58-67. https://doi.org/10.1016/j.compstruct.2016.12.060.

[35] Sun J., Dong Z., Wang X., Wang Y., Qin Y., Kang R. (2020) Simulation and experimental study of ultrasonic cutting for aluminum honeycomb by disc cutter. Ultrasonics; 103:1-8. https://doi.org/10.1016/j.ultras.2020.106102.

[36] Nasir MA, Khan Z, Farooqi I, Nauman S, Anas S, Khalil S, et al. (2015) Transverse shear behavior of a nomex core for sandwich panels. Mech Compos Mater;50:733–8. https://doi.org/10.1007/s11029-015-9462-2.

[37] Paris F, Jackson KE. (2001) A study of failure criteria of fibrous composite materials..

[38] Padhi GS, Shenoi RA, Moy SSJ, Hawkins GL. (1997) Progressive failure and ultimate collapse of laminated composite plates in bending. Compos Struct;40:277–91. https://doi.org/10.1016/S0263-8223(98)00030-0.

[39] Perillo, G., Vedvik, N. P., Echtermeyer, A. T. (2011). Numerical application of three-dimensional failure criteria for laminated composite materials. Department of Engineering Design and Materials, Norwegian University of Science and Technology (NTNU), 5-6.

[40] Guo-dong , Jun L, Bao-lai W. (2009) Progressive damage and nonlinear analysis of 3D four-directional braided composites under unidirectional tension. Compos Struct;89:126–33. https://doi.org/10.1016/j.compstruct.2008.07.016.

[41] Zhao L, Qin T, Chen Y, Zhang J. (2014) Three-dimensional progressive damage models for cohesively bonded composite joint. J Compos Mater;48:707–21. https://doi.org/10.1177/0021998313477169.

[42] Zenia S. (2017) Modélisation numérique de l'usinage des matériaux composites à matrice polymère et fibres longues de carbone. PhD thesis, Université de Lorraine.

[43] Zenia S, Ben Ayed L, Nouari M, Delamézière A. (2015) Numerical prediction of the chip formation process and induced damage during the machining of carbon/epoxy composites. Int J Mech Sci; 90:89–101. https://doi.org/10.1016/j.ijmecsci.2014.10.018.

[44] Lasri L, Nouari M, Mansori M El. (2009) Modelling of chip separation in

machining unidirectional FRP composites by stiffness degradation concept. Compos Sci Technol ;69:684–92. https://doi.org/10.1016/j.compscitech.2009.01.004.

[45] Boutrih L, Ayed L Ben, Nouari M. (2021) Modeling of the interface delamination process when machining hybrid multi-material assemblies. Int J Adv Manuf Technol. https://doi.org/10.1007/s00170-020-06531-z.

[46] Liu PF, Zheng JY. (2008) Progressive failure analysis of carbon fiber/epoxy composite laminates using continuum damage mechanics. Mater Sci Eng A;485:711–7. https://doi.org/10.1016/j.msea.2008.02.023.

[47] Gemkow KS, Vignjevic R. (2013) Strain-softening in continuum damage models : Investigation of MAT _ 058. 9th Euopean LS-DYNA Conf.

[48] Sheikh-Ahmad JY. (2009) Machining of polymer composites. Springer.

[49] Wang XM, Zhang LC. (2003) An experimental investigation into the orthogonal cutting of unidirectional fibre reinforced plastics.pdf. Int J Mach Tools Manuf;43:1015–1022.

[50] Chai GB, Zhu S. A (2011) Review of Low-velocity Impact on Sandwich Structures. Proceedings of the Institution of Mechanical Engineers, Part L: Journal of Materials: Design and Applications, n.d.:1–54.

[51] Jaafar M, Atlati S, Makich H, Nouari M, Moufki A, Julliere B, (2017) A 3D FE Modeling of Machining Process of Nomex® Honeycomb Core: Influence of the Cell Structure Behaviour and Specific Tool Geometry. Procedia CIRP;58:505–10. https://doi.org/10.1016/j.procir.2017.03.255.